

The robustness in identifying and quantifying high-redshift bars using JWST observations

Xinyue Liang¹, Si-Yue Yu^{2,3}, Taotao Fang¹, and Luis C. Ho^{4,5}

¹ Department of Astronomy, Xiamen University, Xiamen, Fujian 361005, People's Republic of China

² Max-Planck-Institut für Radioastronomie, Auf dem Hügel 69, 53121 Bonn, Germany
e-mail: phyyueyu@gmail.com, si-yue.yu@ipmu.jp

³ Kavli Institute for the Physics and Mathematics of the Universe (WPI), The University of Tokyo Institutes for Advanced Study, The University of Tokyo, Kashiwa, Chiba 277-8583, Japan

⁴ The Kavli Institute for Astronomy and Astrophysics, Peking University, 5 Yiheyuan Road, Haidian District, Beijing, 100871, China

⁵ Department of Astronomy, Peking University, 5 Yiheyuan Road, Haidian District, Beijing, 100871, China

May 21, 2024

ABSTRACT

Understanding the methodological robustness in identifying and quantifying high-redshift bars is essential for studying their evolution with the *James Webb* Space Telescope (JWST). We used nearby spiral galaxies to generate simulated images at various resolutions and signal-to-noise ratios, and obtained the simulated galaxy images observed in the Cosmic Evolution Early Release Science (CEERS) survey from Yu et al. Through a comparison of measurements before and after image degradation, we show that the bar measurements for massive galaxies remain robust against noise. While the measurement of the bar position angle remains unaffected by resolution, the measured bar ellipticity is significantly underestimated in low-resolution images. The size measurement is on average barely affected as long as the intrinsic bar size $a_{\text{bar, true}} > 2 \times \text{FWHM}$. To address these effects, correction functions are derived. We also find that the effectiveness of detecting bars remains at $\sim 100\%$ when the $a_{\text{bar, true}}/\text{FWHM}$ is above 2, below which the rate drops sharply, quantitatively validating the effectiveness of using $a_{\text{bar, true}} > 2 \times \text{FWHM}$ as a bar detection threshold. We analyze a set of simulated CEERS images, which take into account observational effects and plausible galaxy (and bar-size) evolution models, and show that a significant (and misleading) reduction in detected bar fraction with increasing redshift would apparently result even if the true bar fraction remained constant. Our results underscore the importance of disentangling the true bar fraction evolution from resolution effects and bar size growth.

Key words. galaxies: high-redshift – galaxies: structure – galaxies: evolution

Use \titlerunning to supply a shorter title and/or \authorrunning to supply a shorter list of authors.

1. Introduction

A galactic bar is a linear elongated stellar structure spanning the center of a disk galaxy. In the local Universe, there are $\sim 70\%$ of disk galaxies hosting a bar when viewed in optical or near-infrared (NIR) wavelengths (e.g. Menéndez-Delmestre et al. 2007; Marinova & Jogee 2007; Aguerri et al. 2009; Ho et al. 2011; Buta et al. 2015; Erwin 2018; Yu et al. 2022a). The bar fraction may vary with Hubble types, stellar mass, and color index (Nair & Abraham 2010; Barazza et al. 2008; Díaz-García et al. 2016; Erwin 2018). It is generally accepted that stellar bars play an important role in galaxy evolution. The non-axisymmetric bar gravitational potential drives cold gas flow toward the galaxy center along the bar's dust lane, enhancing central star formation and leading to the growth of pseudo bulges (Athanasoula 1992, 2002; Athanasoula et al. 2005; Kormendy & Kennicutt 2004; Athanasoula et al. 2005; Jogee et al. 2005; Ellison et al. 2011; Wang et al. 2012, 2020; Gadotti et al. 2020; Yu et al. 2022b,a). Meanwhile, bars reshape galaxy morphology by rearranging the mass distribution, forming substructures such as disk break, spiral arms, and rings (e.g., Knapen et al. 1995; Kormendy & Kennicutt 2004; Ellison et al. 2011; Erwin & Debattista 2013; Gadotti et al. 2020).

Through observations from the *Hubble* Space Telescope (HST), the bar fraction is found to evolve with redshift. Early

HST study by Abraham et al. (1999) reported a decline in the bar fraction towards higher redshifts (see also Abraham et al. 1996; van den Bergh et al. 1996), while later Elmegreen et al. (2004) and Jogee et al. (2004) found that the bar fraction remains consistent up to $z \approx 1$. With the dataset of a considerably large sample covering a wide mass range, Sheth et al. (2008) demonstrated that the bar fraction decreases from 65% at $z = 0.2$ to 20% at $z = 0.84$ (see also Cameron et al. 2010). The declining trend was further confirmed by Melvin et al. (2014) using visual classifications from the Galaxy Zoo (Willett et al. 2013). By studying barred galaxies at $0.2 < z \leq 0.835$, Kim et al. (2021) found that normalized bar sizes do not exhibit any clear cosmic evolution, implying that bar and disk evolution are closely intertwined throughout time. Simulation work by Kraljic et al. (2012) showed that the bar fraction drops to nearly zero at $z \approx 1$, suggesting bars providing as a tool to identify the transition epoch between the high-redshift merger-dominated or turbulence-dominated disks and local dynamically settled disks. Nevertheless, a recent study on the IllustrisTNG galaxies found that the bars appear as early as at $z = 4$ and the bar fraction evolves mildly with cosmic time (Rosas-Guevara et al. 2022). They argued that if only considering long bars their results can reconcile with the observation studies as those can suffer from resolution effects.

Analysing bar structures in galaxies at high redshift using HST observations present a considerable challenge. For galaxies at $z \gtrsim 2$, imaging through the HST F814W filter observes the rest-frame ultraviolet, a wavelength where bars are often less visible (Sheth et al. 2003). The HST NIR F160W imaging possesses a relatively broader point spread function (PSF), making it inadequate for resolving bar structures at high redshift. In addition, the depth of HST observations might be insufficient for detecting the outer regions of high-redshift galaxies, causing galaxies with a long bar to resemble edge-on galaxies. The *James Webb* Space Telescope (JWST) delivers images with unparalleled sensitivity and resolution in NIR, significantly enhancing our understanding of galaxy structures at high redshift. Recent JWST studies have revealed a significant fraction of regular disk galaxies at high redshift (Ferreira et al. 2022a,b; Kartaltepe et al. 2023; Nelson et al. 2022; Robertson et al. 2023; Jacobs et al. 2023; Xu & Yu 2024). This result contrasts with the findings from HST-based studies, which predominantly identified peculiar galaxies at $z > 2$ (e.g., Conselice et al. 2008; Mortlock et al. 2013). Remarkably, barred galaxies at $z \approx 2$ –3, previously undetected in HST observations, have now been identified using JWST (Guo et al. 2023; Le Conte et al. 2024; Costantin et al. 2023).

Although JWST imaging offers exceptional angular resolution, when observing high-redshift galaxies, its physical resolution is still lower than that achieved with ground-based observations of nearby galaxies. This complicates direct comparisons between bars observed in low-redshift and high-redshift galaxies, making the study of bar evolution less straightforward. Sheth et al. (2003) pointed out that the bar fraction calculated using low-resolution images tends to be underestimated. This underestimation is likely to be exacerbated by the bar size evolution, wherein bars become shorter in physical size at higher redshift as predicted in numerical simulations (e.g., Debattista & Sellwood 2000; Martínez-Valpuesta et al. 2006; Athanassoula 2013; Algorry et al. 2017). In contrast, the influence of cosmological surface brightness dimming on bar detection is minimal (Sheth et al. 2008). By analysing apparent the bar sizes in galaxies from the Spitzer Survey of Stellar Structure in Galaxies (S⁴G; Sheth et al. 2010), Erwin (2018) showed that most of the projected bar radii are larger than twice the PSF full width at half-maximum (FWHM) and thus suggested this value as the bar detection threshold. Such a threshold successfully reconciles the difference in the dependency of bar fraction on parameters like stellar mass or gas fraction, especially when comparing their results with studies based on low-resolution SDSS images (Masters et al. 2012; Oh et al. 2012; Melvin et al. 2014; Gavazzi et al. 2015). Likewise, based on extensive experiments on artificial galaxies, Aguerrí et al. (2009) suggested that the limitation of bar detection is 2.5 times FWHM. Nevertheless, the threshold bar size for bar detection have not yet been validated in a quantitative way based on real images, especially under typical JWST observational conditions. Resolution may also impact measured bar properties, such as size, ellipticity, and position angle, which are frequently employed to study the formation and evolution of bars (e.g., Elmegreen et al. 2007; Gadotti 2011; Kim et al. 2021; Yu et al. 2022a). While it seems intuitive that bar ellipticity would be underestimated due to PSF smoothing as spatial resolution deteriorates, the exact impact and the influence on other parameters remain largely unexplored.

It is therefore nontrivial to interpret the observational results obtained from JWST without knowing the systematics caused by the observation limitations. To disentangle the potential intrinsic relations or evolution for bars from the observation effects, in the current work we aim to understand how the observa-

tional factors can influence the identification and quantification of bars. Recently, by accounting for observational effects and galaxy evolution, Yu et al. (2023) used a sample of nearby galaxies to create images of simulated high-redshift galaxies as would be observed by JWST in the Cosmic Evolution Early Release Science (CEERS) survey (PI: Finkelstein, ID=1345, Finkelstein et al. 2022; Bagley et al. 2023). In addition to the simulated galaxies CEERS images provided by Yu et al. (2023), we employ their sample of nearby galaxies to produce images at low resolutions for a given S/N and at low S/N for a given resolution. Then we compare the measurements before and after image degradation to understand the robustness in analysing bars in high-redshift galaxies observed with JWST. The structure of this paper is as follows. Section 2 presents an overview of the dataset. Section 3 describes the procedure for generating images mimicking the JWST resolution and S/N . In Section 4, we present the robustness of bar structure measurements under JWST observation. We discuss the implication of our results in Section 5. A summary is given in Section 6. Throughout this work, we use AB magnitudes and assume the following cosmological parameters: $(\Omega_M, \Omega_\Lambda, h) = (0.27, 0.73, 0.70)$.

2. Observational material

We construct our sample to study the robustness in identifying and quantifying bars based on the nearby galaxies sample defined in Yu et al. (2023). By restricting to luminosity distance (D_L) of $12.88 \leq D_L \leq 65.01$ Mpc, stellar mass (M_*) of $10^{9.75-11.25} M_\odot$, and excluding images severely contaminated by close sources, Yu et al. (2023) select 1816 galaxies from the Siena Galaxy Atlas¹ (SGA; Moustakas et al. 2021) that is made up of 383,620 galaxies from the Dark Energy Spectroscopic Instrument (DESI) Legacy Imaging Surveys (Dey et al. 2019). Out of the 1816 galaxies, we select 448 face-on spiral galaxies by requiring that the galaxies are available in the third Reference Catalog of Bright Galaxies (RC3; de Vaucouleurs et al. 1991), and have Hubble type of $T > 0.5$ and axis ratio of $b/a > 0.5$. We exclude S0s because they are much rarer at high redshifts than in the local universe (e.g., Postman et al. 2005; Desai et al. 2007; Cavanagh et al. 2023), their bars are significantly different from those in spirals (e.g., Aguerrí et al. 2009; Buta et al. 2010; Díaz-García et al. 2016), and distinguishing them from Es is challenging with limited image quality. The median angular luminosity distance and the typical DESI r -band FWHM of our sample is 43 Mpc and 0.9 arcsec, respectively. Thus the FWHM translates to a typical linear resolution of 0.2 kpc. Considering the high quality of linear resolution of the DESI images and the typical bar size range of 0.5–10 kpc found in nearby galaxies (Erwin 2005; Díaz-García et al. 2016), the bar structures are effectively spatially resolved in our nearby galaxy sample. We use the star-cleaned r -band images provided by Yu et al. (2023) for the our analysis, as the NIRCcam of JWST will trace the rest-frame optical light at high redshifts. The star-cleaned images are essential for the creation of images of various resolution and S/N levels observed by JWST. These images are generated by replacing the flux emitted by sources other than the target galaxy with interpolated flux or flux in the rotational symmetric regions (details see Yu et al. 2023).

Several methods have been established to identify bars and measure their properties, including visual inspection (e.g., de Vaucouleurs et al. 1991; Nair & Abraham 2010; Herrera-Endoqui et al. 2015), ellipse fitting method (e.g., Menéndez-

¹ <https://www.legacysurvey.org/sga/sga2020/>

Delmestre et al. 2007; Marinova & Jøgee 2007; Sheth et al. 2008; Yu & Ho 2020), Fourier Analysis (e.g., Ohta et al. 1990; Elmegreen & Elmegreen 1985; Aguerri et al. 1998), and two dimensional decomposition (e.g., Gadotti 2009; Laurikainen et al. 2005; Salo et al. 2015). There are always limitations and potential uncertainties associated with these techniques, and no single method can guarantee perfect results (Athanasoula & Misiriotis 2002; Aguerri et al. 2009; Lee et al. 2019). We use ellipse fitting method to analyze bars. The isophote ellipticity (ϵ) has been shown to increase with radius within regions dominated by bars, beyond which the ϵ would drop (Menéndez-Delmestre et al. 2007; Aguerri et al. 2009). However, in some barred galaxies, especially the SAB galaxies (which represent an intermediate class between spirals and those with strong bars), this drop in the ϵ profile can be absent, as the bar is not strictly straight, reducing the difference in ϵ between the bar and underlying disk. Another point to consider is the observational effect. For galaxies observed at high redshifts, the drop in the ϵ profile can be smoothed out by the PSF, as will be illustrated in Fig. 2, 3, and 5. Therefore, we adopt the strategy suggested by Erwin & Sparke (2003) to seek out peaks in the ϵ profile as a signature of bars or potential bar candidates. While this approach is effective, we opted not to account for possible twists in the position angle (PA) profile, but supplement our approach with visual inspections to ascertain the presence of bars.

We use the `ellipse` task from `photutils`² twice for each image to perform isophote fitting. First, we set the center, ϵ , and PA as free parameters and then determine the galaxy center by averaging the centers of the resulting isophotes in the inner region. Second, we fix the center to derive the profiles of ϵ and PA. For each ϵ profile, we select the bar candidates by search for local peaks greater than 0.1 in the ϵ profile. For each bar candidate, we visually check if it represents a bar instead of dust lanes, star forming regions, or spiral arms. If one of the candidates is confirmed as a bar, the galaxy is classified as barred galaxies and the semi-major axis (SMA), ϵ , and PA corresponding to the selected peak (denoted as $a_{\text{bar, true}}$, $\epsilon_{\text{bar, true}}$, and $\text{PA}_{\text{bar, true}}$, respectively) are taken as the measures of the bar properties. The subscript of “true” is used to distinguish these values from those obtained by analyzing simulated degraded images in Sect. 3. The $a_{\text{bar, true}}$ describes the apparent bar size. For several galaxies where a bar is obvious by visual inspection, the ϵ profile doesn’t exhibit a peak because the ellipticity of the bar is comparable to that of the disk. We manually determine the SMA that best characterizes the bar and subsequently estimate its properties. The remaining galaxies are classified as unbarred galaxies.

Out of 448 spiral galaxies, 304 are classified as barred, yielding a bar fraction of 68% that, albeit being slightly lower, is consistent with previous studies identifying bars through visual inspection (e.g., de Vaucouleurs et al. 1991; Marinova & Jøgee 2007; Buta et al. 2015). This fraction is marginally higher than those found in some studies using ellipse fitting methods (e.g., Barazza et al. 2008; Aguerri et al. 2009), which have missed barred galaxies, especially the SAB types, that don’t exhibit a sudden drop in their ϵ profiles. This calculated bar fraction of 68% is denoted as $f_{\text{bar, true}}$. Figure 1 summarizes the basic bar properties in our sample. The distribution of $\epsilon_{\text{bar, true}}$ is shown in the left panel, and the relationship between $a_{\text{bar, true}}$ and galaxy stellar mass is displayed in the right panel. Our sample covers a wide range of bars, with $\epsilon_{\text{bar, true}}$ values spanning from 0.25 to 0.85 and $a_{\text{bar, true}}$ ranging from 0.3 to 10 kpc. We demonstrate that more massive galaxies have longer $a_{\text{bar, true}}$, consistent with pre-

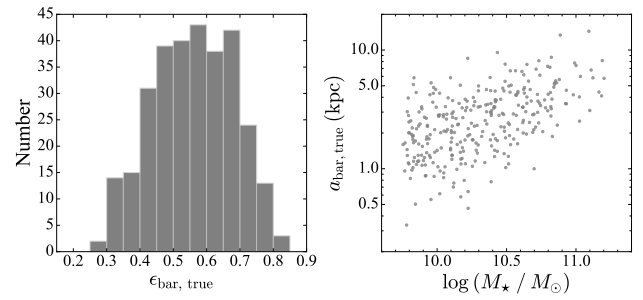


Fig. 1. Basic properties of the barred galaxies in our sample. The left panel illustrates the distribution of ellipticity of bars ($\epsilon_{\text{bar, true}}$), while the right panel shows the projected bar size as semi-major axis ($a_{\text{bar, true}}$) versus stellar mass (M_{\star}).

vious work (e.g. Díaz-García et al. 2016; Erwin 2019; Kim et al. 2021), though our analysis does not involve the deprojection process for the bars. We refer to these properties derived from DESI images as the true bar properties due to the high quality of the DESI images.

3. Image simulations

Two approaches are employed to investigate the cosmological redshift effects on the detection and measurement of bars at high redshift with JWST. The first approach, for considering observational effects, is to use the r -band star-cleaned image of nearby galaxies to generate and study simulated images of various resolution and S/N (Sect. 3.1 and Sect. 3.2). In the second approach, we analyse the simulated CEERS images that were created by taking into account for both observational effects and galaxy evolutions (Sect. 3.3). We re-identify and re-measure the bars present in these simulations to illustrate how resolution, noise, and their combined effects influence the analysis of bars in galaxies at high redshifts.

3.1. Simulated low-resolution images

The detectability of the bar is often gauged by the ratio of $a_{\text{bar, true}}$ to PSF FWHM, that is $n = a_{\text{bar, true}}/\text{FWHM}$, however, the quantitative impact of this ratio remains to be elucidated. To observe rest-frame optical wavelength, we assume using the F115W, F150W, and F200W filters for studying bars in real observations at redshifts of $z < 1$, $1 \leq z < 2$, and $2 \leq z < 3$, respectively. Although the JWST F115W images can better resolve bar structures owing to their narrower PSF, they may miss bars at high redshifts due to a shift toward shorter rest-frame wavelengths. Consequently, the redder filters are utilized to mitigate this effect. We thus examine three JWST PSFs corresponding to the filters F115W, F150W, and F200W, which have FWHMs of 0.037, 0.049, and 0.064 arcsec, respectively³. A pixel scale of 0.03 arcsec/pixel, consistent with the CEERS data release (Bagley et al. 2023), is adopted.

To generate low-resolution images for understanding the impact of PSF smoothing, we start by downsizing the star-cleaned images to match an exponentially increasing sequence of n values: 1.0, 1.2, 1.44, 1.73, 2.07, 2.49, 2.99, 3.58, 4.3, 5.16, and 10. Correspondingly, the DESI PSFs are resized using the same scaling factor. Next, we generate JWST PSFs using `WebbPSF` (Per-

³ <https://jwst-docs.stsci.edu/jwst-near-infrared-camera/nircam-performance/nircam-point-spread-functions>

² <https://photutils.readthedocs.io>

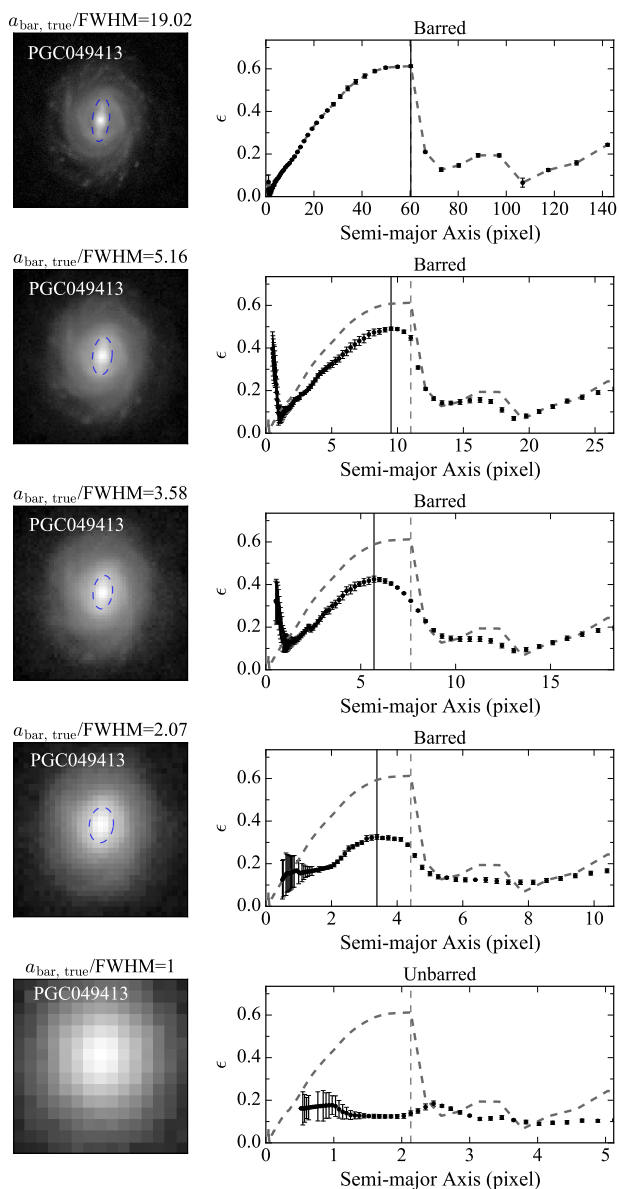


Fig. 2. Illustration of the impact of decreasing resolution on the bar analysis, using PGC049413 as an example. On the left are the galaxy images, with their respective derived ϵ profiles to the right. At the top of each image, the ratio of $a_{\text{bar, true}}/\text{FWHM}$ is indicated. The first row shows the results from DESI, succeeded by the results from low-resolution F200W images in the rows below. The DESI ϵ profiles are plotted with grey dashed curves in the right panels, with the intrinsic bar position denoted as a grey vertical dashed line. When a bar is successfully identified, it is marked on the image by an ellipse and indicated on the profile by a vertical solid line.

rin et al. 2014) and derived a kernel via Fourier transformation to transform the resized PSF to the JWST PSF. Lastly, we convolve the downsized galaxy image with the kernel to obtain the simulated low-resolution image. These simulated images have a very high S/N , allowing us to focus on examining the impacts of the PSF. We analyse the bar structure in each low-resolution image using the same ellipse fitting method outlined in Sect. 2. The derived bar size, ellipticity, and position angle are denoted as a_{obs}^n , ϵ_{obs}^n , and PA_{obs}^n .

Figure 2 uses PGC049413 as an example to illustrate the impact of decreasing resolution on the bar analysis, when the

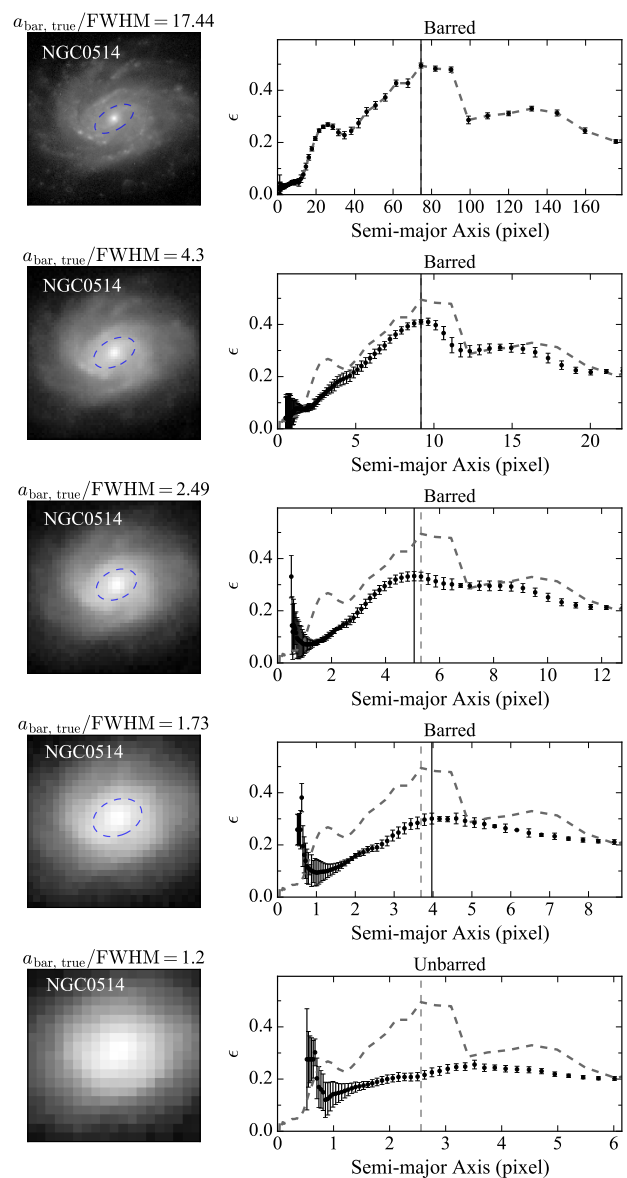


Fig. 3. Illustration of the impact of decreasing resolution on the bar analysis, using NGC0514 as another example. Details are the same as Fig. 2.

F200W PSF is considered. The images are shown in the left column, while the ϵ profiles are shown on the right. The top row shows the result derived from the DESI image. As the DESI image has quite high resolution, indicated by $a_{\text{bar, true}}/\text{FWHM} = 19.02$, there is clearly a bar in the image and a peak or equivalently a drop in the ϵ profile. The peak or the drop, marked by the solid line in the profile, is selected to measure the bar. An ellipse with the resulting parameters is plotted on the image to illustrate the measurement. The subsequent rows present the results obtained from the simulated low-resolution images. To facilitate the comparison between the results before and after resolution degradation, we adjust the SMA of the DESI ϵ profile to match those from the low-resolution images, and then plot the adjusted profiles as grey dashed curves and intrinsic bar size as the vertical dashed line. As the resolution decreases to $a_{\text{bar, true}}/\text{FWHM} = 5.16$ and 3.58 , the bar structures in the images remain clearly visible despite the increasing blur. The

persistent peak in the ϵ profile underscores the presence of the bar, though its amplitude decreases. This reduced peak amplitude indicates an underestimation of bar ellipticity. Meanwhile, the peak shifts inward, leading to an underestimation of measured bar size. Moreover, the sudden drop seen in the DESI ϵ profile softens at $a_{\text{bar, true}}/\text{FWHM} = 5.16$ and is completely absent at $a_{\text{bar, true}}/\text{FWHM} = 3.58$. This behavior leads us to use peak in ϵ profiles to identify bars, as described in Sect. 2. These changes in the image and the ϵ profiles are caused by the PSF convolution, which rounds the bar structure and reduces its clarity at the edges. When the resolution decreases to $a_{\text{bar, true}}/\text{FWHM} = 2.07$, the image becomes more unclear, causing subtle structural details like spiral arms to significantly fade. However, the bar structure remains discernible in the image with a distinct peak in the ϵ profile. When the resolution further decreases to $a_{\text{bar, true}}/\text{FWHM} = 1$, the image has become so blurred that any structure is completely invisible and the characteristic features corresponding to a bar in the ϵ profile disappears.

For simulated images of PGC049413, we note the significant decrease in the measured bar size. At $a_{\text{bar, true}}/\text{FWHM} = 3.58$, the fractional difference between measured and intrinsic bar size yields -25% . However, such cases are not typical. On average, lower resolution only reduces the measured bar size by a few percent when $a_{\text{bar}}/\text{FWHM} > 2$, as will be discussed in detail in Sect. 4. Figure 3 uses NGC0514, a SAB galaxy, as an example to illustrate the typical resolution effect. At $a_{\text{bar, true}}/\text{FWHM} = 4.3$, the bar size still matches the original size, while at $a_{\text{bar, true}}/\text{FWHM} = 2.49$, the observed bar size is reduced by 5% . However, at $a_{\text{bar, true}}/\text{FWHM} = 1.73$, the bar size is overestimated due to the image being blurred, causing part of the spiral structure to be recognized as the bar. At $a_{\text{bar, true}}/\text{FWHM} = 1.2$, the bar structure is completely lost. Additionally, similar to the previous illustration of PGC049413, the amplitude of the ϵ profile gradually decreases as the resolution worsens.

3.2. Simulated low- S/N images

To explore the influence of noise on the bar analysis under realistic observational conditions in CEERS, we first estimate the S/N range of the galaxy images observed in the survey. We use the science data, error map, and source mask from the CEERS Data Release Version 0.6 (data reduction sees Bagley et al. 2023)⁴. We use the catalog of Stefanon et al. (2017) to select galaxies with stellar mass $M_{\star} \geq 10^{9.75} M_{\odot}$ at redshifts of $0.75 \leq z \leq 3.0$, and then use *sep* (Bertin & Arnouts 1996; Barbary 2016) to generate a mask for each galaxy. Images of galaxies that are severely contaminated by close sources are excluded. We calculate the sky uncertainty through *Autoprof* (Stone et al. 2021) and derive the galaxy flux uncertainty from the error map. We calculate the map of S/N for each galaxy by dividing the galaxy flux by the flux uncertainty pixel by pixel, and compute average S/N over an elliptical aperture with SMA of galaxy Petrosian radius, and with galaxy ϵ and PA. This average S/N value is considered as the S/N of this galaxy. The rationale for calculating the S/N averaged over the pixels occupied by the galaxy, instead of simply dividing the total galaxy flux by its uncertainty (which treats the galaxy like a point source), is that the S/N of individual pixels can vary throughout the galaxy. Since bars are extended structures, averaging the S/N over the pixels that encompass the bars provides a more accurate representation of the signal strength of the bars relative to the noise.

As a result, for CEERS galaxies observed in the F115W ($0.75 < z < 1$), F150W ($1 < z < 2$), and F200W ($2 < z < 3$) filters, the median S/N values are 20.0, 11.4, and 10.0, respectively. The corresponding standard deviations are 11.5, 9.5, 9.0. Moreover, over 95% of galaxies in each filter exhibit a S/N greater 3. Therefore, to investigate whether and how the typical noise level in CEERS influences our bar analysis, we use the high- S/N simulated image of $a_{\text{bar, true}}/\text{FWHM} = 4.3$ to generate, for each galaxy, simulated images with an exponentially increasing S/N : 3, 4.2, 5.9, 8.2, 11.5, 16.1, 22.6, 31.6, 44.3, and 62.0. The ratio $a_{\text{bar, true}}/\text{FWHM}$ is fixed for isolating the noise effect. We have verified that using images of other $a_{\text{bar, true}}/\text{FWHM}$ to examine noise effects does not significantly affect our results. To make the image noisy, we rescale the image flux with a scaling factor, derive flux noise, and add the flux noise as well as a background map to the flux-rescaled image. In this process, we use the median ratio of galaxy flux to flux variance and the patch of cleaned real CEERS background, as provided by Yu et al. (2023), to compute the galaxy flux noise and to represent the background map, respectively. The scaling factor is iteratively adjusted to match our desired S/N . We apply the same ellipse fitting method as described in Sect. 2 to identify and quantify bars. The derived bar size, ellipticity, and position angle from these images of various S/N are denoted as $a_{\text{obs}}^{S/N}$, $\epsilon_{\text{obs}}^{S/N}$, and $\text{PA}_{\text{obs}}^{S/N}$.

With the layout consistent with Fig. 2, Fig. 4 uses PGC049413 as an example to illustrate the impact of noise. When $S/N \geq 16.1$ (top four rows), noise hardly affects the images, keeping the bar structure clear and the corresponding ϵ profiles unchanged. As the S/N drops to 8.2 and further to 3 (bottom two rows), the influence of noise becomes a bit more significant, resulting in a decrease in image clarity and greater uncertainty in the ϵ profile. Despite this, the bar structure is still discernible, and the general shape of the ϵ profiles undergoes only minor change. Measurements of the bar size and ellipticity from images with low S/N are consistent with those from images with high S/N . Therefore, the bar identification and quantification for PGC049413 are not significantly affected by the noise within the typical S/N range observed in the CEERS field.

3.3. Simulated galaxy images observed in CEERS

To examine the cosmological redshift effect, that is a combination of resolution and noise effects in a specific way, simulated CEERS images with both observational effects and evolution effects considered are essential. Yu et al. (2023) used multi-wavelength images of a sample of nearby DESI galaxies to generate artificially redshifted images observed in JWST CEERS at $z = 0.75, 1.0, 1.25, 1.5, 1.75, 2.0, 2.25, 2.5, 2.75$, and 3.0 . The F115W filter is used for $z = 0.75$ and 1 , the F150W filter is used for $z = 1.25, 1.5$, and 1.75 , and the F200W filter is used for $z = 2.0$ to 3.0 . Their image simulation procedure involves spectral change, cosmological surface brightness dimming, luminosity evolution, physical disk size evolution, shrinking in angular size due to distance, decrease in resolution, and increase in noise level (for details, see Yu et al. 2023). In particular, PSFs are matched to those generated using *WebbPSF* and a cleaned blank CEERS background is employed. A bar evolution model is incorporated. With increasing redshift, the physical size of bars becomes shorter as the disk size becomes smaller following the galaxy size evolution derived by van der Wel et al. (2014). Applying a galaxy evolution model is a separate, additional consideration, apart from the basic resolution and S/N effects. This dataset fits our scientific goal of understanding the

⁴ <https://ceers.github.io/dr06.html>

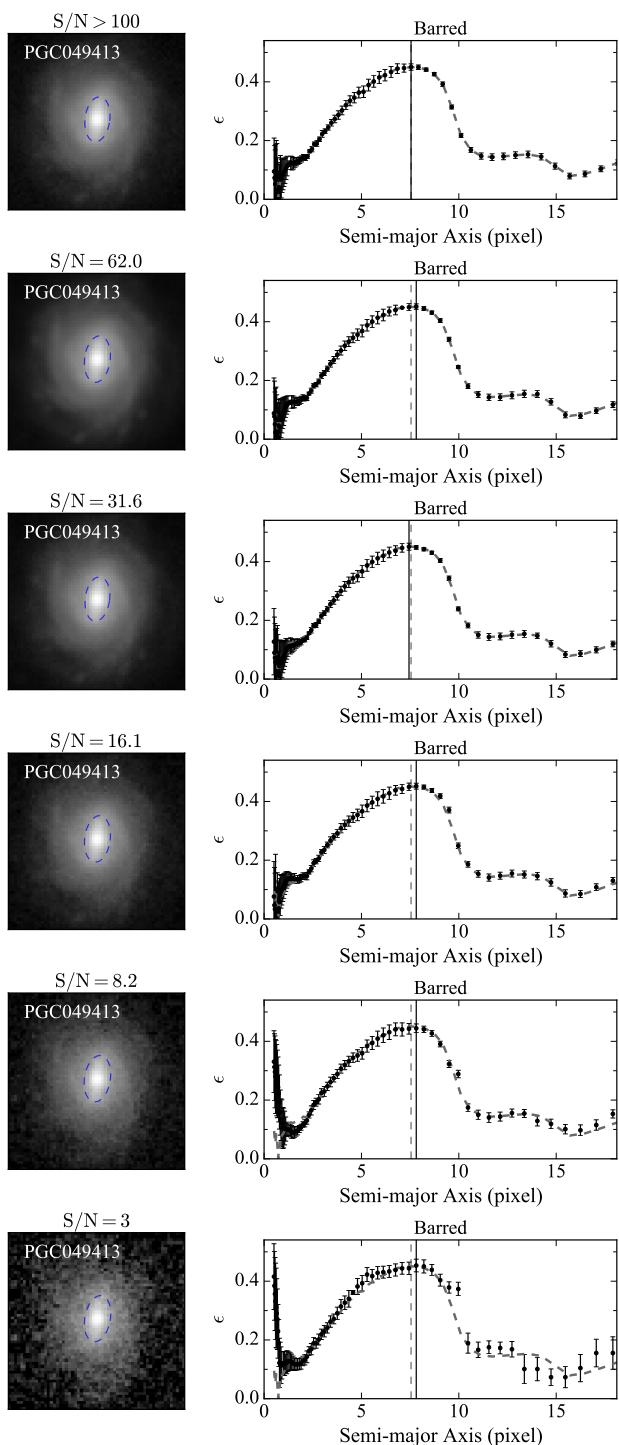


Fig. 4. Illustration of the impact of noise on the bar analysis. The symbols are consistent with Fig. 2. The top row now displays the noiseless simulated image of $a_{\text{bar, true}}/\text{FWHM} = 4.3$ and its profile, while the subsequent rows show the simulated low- S/N images and their profiles.

redshift effects on the bar measurements. We analyze each simulated CEERS image using the ellipse fitting method described in Sect. 2. The resultant bar size, ellipticity, and position angle are denoted as a_{obs}^z , ϵ_{obs}^z , and PA_{obs}^z .

Figure 5 showcases the redshift effects on bar measurement. The top row displays results derived from the DESI image, while the subsequent rows present those from the simulated CEERS

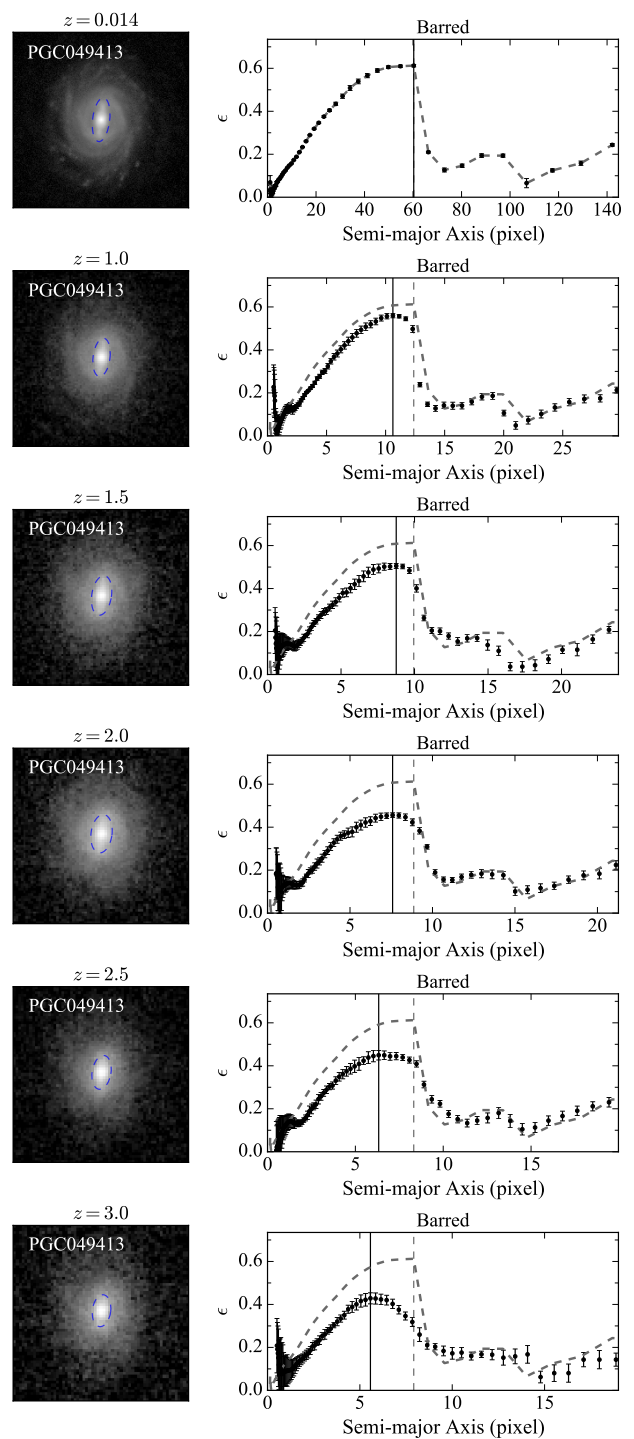


Fig. 5. Illustration of the impact of redshift effects on the bar analysis. The redshift effects include observational effects and galaxy (and bar) evolution. The symbols are consistent with Fig. 2, except that simulated CEERS images at various redshifts and their results are shown.

images at high redshifts. The galaxy structures in the DESI image are clear and the drop or peak in the ϵ profile is prominent. When the galaxy is artificially moved to $z = 1$ and then further to $z = 3$, the galaxy image becomes increasingly blurred and noisy. Meanwhile, the ϵ profiles tend to flatten, with the sudden drop in the ϵ profile disappearing entirely at $z \geq 1.5$. The flattening in the ϵ profiles is due to the decreasing $a_{\text{bar, true}}/\text{FWHM}$ with increasing redshifts, consistent with the expectation based

on the resolution effect discussed in Sect. 3.1. As anticipated from Sect. 3.2, the noise only make the profiles at high redshifts slightly more chaotic than low-redshift results. Together with the results shown in Sections 3.1 and 3.2, Figure 5 suggests that the noise has a minimal impact on the analysis of bars observed in the CEERS field for the mass and redshift ranges we considered, and the resolution effect is the predominant factor. While the peak corresponding to the bar is reduced gradually with increasing redshift, the bar remains detectable both in the image and in the ϵ profile for PGC049413. Nevertheless, it's evident that the difference between bar size and bar ellipticity measured from the simulated high-redshift images and their true values are increasing.

To illustrate the necessity of incorporating galaxy evolutions in generating simulated CEERS images, we created another set of simulated images considering only observational effects without any evolutions. Figure 6 compares the two sets of simulated data using PGC049413 as an example. The left column shows the simulated images without any galaxy evolution models, while the right column shows the simulated images with the galaxy evolution models. As z increases, the bar structure gradually fades due to noise. At $z = 3.0$, the bar is still visible from the simulated CEERS image with evolutions but appears completely faded into the background in images without evolutions. The S/N of the images without evolution models (in intrinsic surface brightness) is significantly reduced due to the cosmological dimming effect on observed galaxy surface brightness, which become fainter by $2.5 \log(1+z)^3$ at high redshifts (AB magnitude is used). However, the intrinsic surface brightness has been found to brighten with increasing redshift (e.g., Barden et al. 2005; Sobral et al. 2013), which is caused by a combination of luminosity evolution and size evolution (Yu et al. 2023). We calculated the S/N for these images and found that, from $z = 1.25$, the S/N falls below 3 and is significantly lower than that for real CEERS images. At $z = 3.0$, the median value of S/N yields only 0.54. The low S/N causes a large number of bars to be undetected. These noisy images are therefore inconsistent with the real CEERS galaxy images presenting quite good S/N to resolve galaxy structures, validating our procedure to generate simulated CEERS images by incorporating galaxy evolution models.

We give a caution that our bar evolution model may not be correct. Our input bar model assume the bar size related to disk size remains unchanged across redshift. Nevertheless, such a ratio changes by a factor of ~ 2 from $z \sim 3$ to 0 in simulations (Anderson et al. 2024). Future studies comparing fraction and size of bars observed in JWST images with simulated images may give a better constraint on the bar evolution model.

4. Measurement robustness of bar structures

As illustrated in Sect. 3 through a representative example, the resolution limitation can significantly influence the identification and quantification of bars observed in the JWST CEERS field, while the effects of noise are minimal. These factors introduce considerable impact for galaxies at high redshifts. In this Section, we quantify these effects using the full sample of 448 galaxies.

4.1. The effect of resolution

As resolution decreases, bars may not be detected. For each set of simulated low-resolution images with the specific value of $a_{\text{bar, true}}/\text{FWHM}$, we determine the method effectiveness of de-

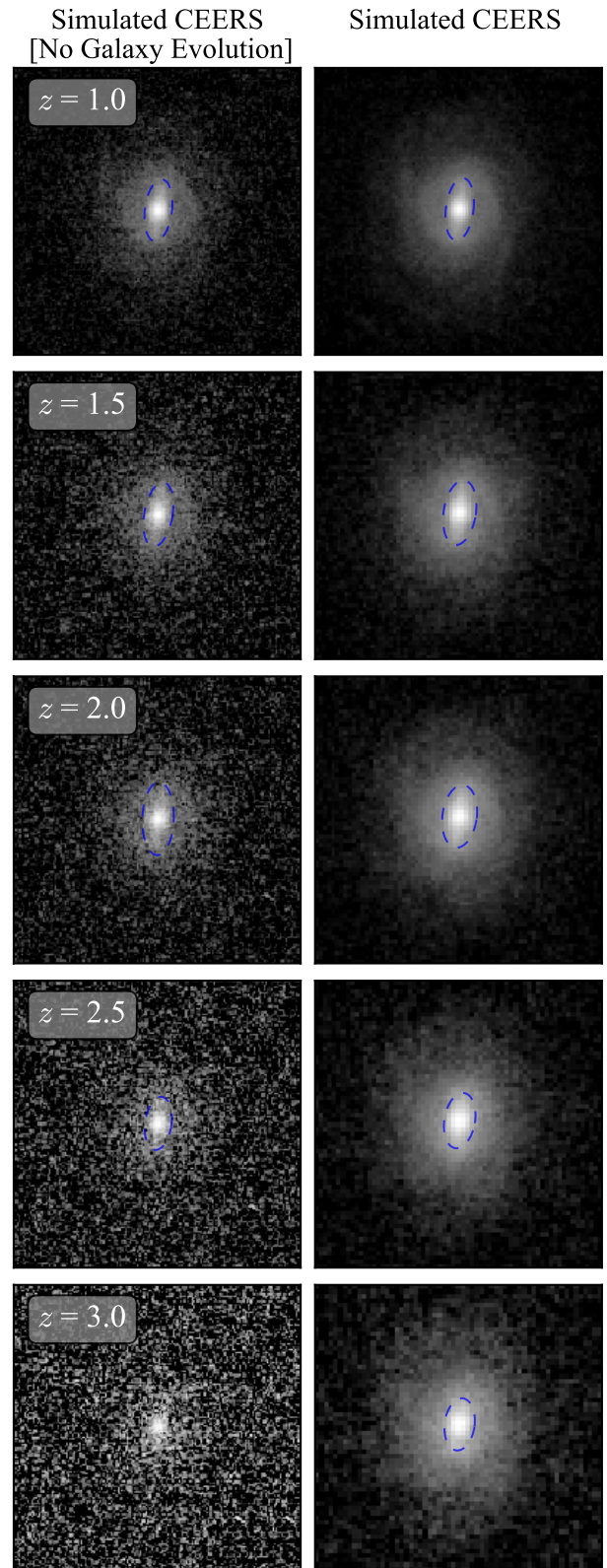


Fig. 6. Illustration of the simulated CEERS image with the adoption of a galaxy evolution model (on the right) as well as the one without (on the left) using PGC049413 as an example, presented as the redshift increases. The blue ellipse marks the detected bar structure in the image if a bar is identified.

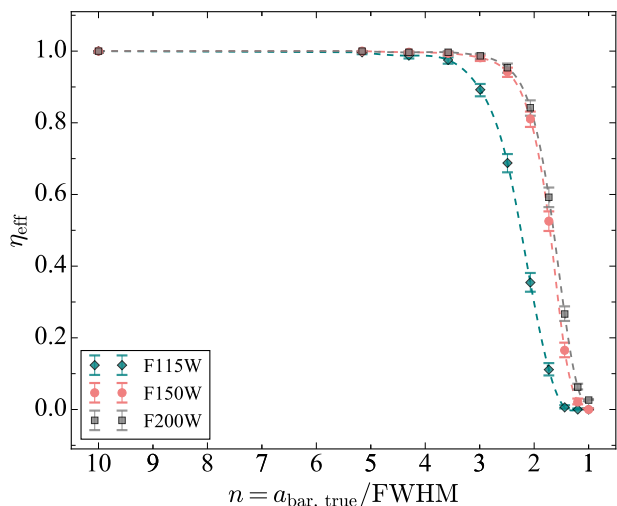


Fig. 7. Effectiveness of the method of detecting bars, η_{eff} , as a function of resolution $n = a_{\text{bar,true}}/\text{FWHM}$. The green diamonds, red circles, and grey squares represent the results based on the F115W, F150W, and F200W filters, respectively.

detecting bars (η_{eff}), defined as:

$$\eta_{\text{eff}} = \frac{\text{Number of detected bars}}{\text{All bars}}. \quad (1)$$

We plot the η_{eff} as a function of resolution ($n = a_{\text{bar,true}}/\text{FWHM}$) in Fig. 7, where the green diamonds, red circles, and grey squares denoting the results for F115W, F150W, and F200W filters, respectively. We calculate the error of each η_{eff} (and bar fraction) using the Wilson interval. With the $a_{\text{bar,true}}/\text{FWHM}$ decreasing from 10 to 1, the η_{eff} declines from 100% to nearly 0. However, the profile shape varies across different bands. For the F115W band, the η_{eff} stays at $\sim 100\%$ until reaching $a_{\text{bar,true}}/\text{FWHM} \approx 3$, after which it experiences a sharp decline. We calculate the $a_{\text{bar,true}}/\text{FWHM}$ corresponding to effectiveness of detecting bars of 50% through interpolation and obtain 2.47. For F150W or F200W band, the η_{eff} does not show the sharp decline until reaching $a_{\text{bar,true}}/\text{FWHM} \approx 2$. For F150W and F200W band, the 50% effectiveness of detecting bars corresponds to $a_{\text{bar,true}}/\text{FWHM} = 1.71$ and 1.65, respectively. Compared to F150W and F200W bands, the F115W-band η_{eff} trend has the sharp drop at higher $a_{\text{bar,true}}/\text{FWHM}$. This is because, given the pixel size of 0.03 arcsec/pixel, the F115W PSF FWHM gives ~ 1.2 pixels, significantly below the 2-pixel threshold required for Nyquist sampling. This inadequacy in sampling causes the F115W image to lose small-scale structure information, leading some short bars to become undetectable. Our results suggest that for images with a Nyquist-sampled PSF (such as JWST PSFs in the F200W, F277W, F356W, and F444W band), the critical bar size for detecting bars is $2 \times \text{FWHM}$, providing a quantitative justification for the empirical choice of $a_{\text{bar,true}} = 2 \times \text{FWHM}$ as the bar size threshold for bar detection by Erwin (2018). Erwin (2018) determine the factor of 2 based on the fact that almost all the bars in the S⁴G sample are larger than $2 \times \text{FWHM}$.

To understand how resolution can quantitatively impact the measured bar properties, we compare the properties (a_{obs}^n , ϵ_{obs}^n , and PA_{obs}^n) derived from the low-resolution images with the intrinsic bar properties ($a_{\text{bar,true}}$, $\epsilon_{\text{bar,true}}$, and $\text{PA}_{\text{bar,true}}$) obtained from DESI images. We use the fractional difference $\Delta a_{\text{obs}}^n / a_{\text{bar,true}}$, where $\Delta a_{\text{obs}}^n = (a_{\text{obs}}^n - a_{\text{bar,true}})$, to quantify the deviation in measured bar size as the resolution,

$n = a_{\text{bar,true}}/\text{FWHM}$, decreases. The number distributions of $\Delta a_{\text{obs}}^n / a_{\text{bar,true}}$ at different n are shown in Fig. 8. Results for the F200W band are shown. In each panel, the n , the mean Δa_{obs}^n , denoted as $\overline{\Delta a/a}$, and the standard deviation of Δa_{obs}^n , denoted as $\sigma_{\Delta a/a}$, are present. The vertical dashed line marks the location of $a_{\text{obs}}^n = a_{\text{bar,true}}$. The overall distribution of $\Delta a_{\text{obs}}^n / a_{\text{bar,true}}$ is approximately symmetric. As the n decreases from 10 to 2.49, the measured bar size tends to be more and more underestimated, though slightly, by from 1% to 6%. Such an underestimation is caused by PSF smoothing as demonstrated in Fig. 2. However, as n decreases from 1.73 to 1, the measured bar size tends to be more and more overestimated with lower resolution, by from 2% to 19%. This can be clarified by the fact that, under relatively poor resolution conditions, various structures such as bars, spiral arms, and disks tend to become mixed. As a result, it becomes challenging to distinguish the bar distinctly, potentially leading to an overestimation of the measured bar size. The $\Delta a_{\text{obs}}^n / a_{\text{bar,true}}$ as a function of n can be found in Fig. 11.

In Fig. 9, we compare the intrinsic bar ellipticity $\epsilon_{\text{bar,true}}$ with the measure bar ellipticity ϵ_{obs}^n that are obtained from images at each resolution level $n = a_{\text{bar,true}}/\text{FWHM}$. The fractional difference is calculated as $\Delta \epsilon / \epsilon = (\epsilon_{\text{obs}}^n - \epsilon_{\text{bar,true}}) / \epsilon_{\text{bar,true}}$. Their mean value ($\overline{\Delta \epsilon / \epsilon}$) and standard deviation ($\sigma_{\Delta \epsilon / \epsilon}$) is indicated in each panel. As the resolution decreases from $n = 10$ to 1, there is a clear trend that the data point distribution gradually shifts towards lower ϵ_{obs}^n . This trend can be quantitatively observed by examining the $\overline{\Delta \epsilon / \epsilon}$, which decreases from -2% to -54% . Our results suggest that the PSF smoothing causes the measured bar ellipticity to be underestimated compared to its intrinsic value, and the underestimation becomes progressively more pronounced as the resolution decreases. The $\Delta \epsilon / \epsilon$ as a function of n can be found in Fig. 11.

Regarding the robustness in measuring the orientation of bars, we compare PA_{obs}^n with $\text{PA}_{\text{bar,true}}$ in Fig. 10. Their mean difference ($\overline{\Delta \text{PA}}$) and standard deviation ($\sigma_{\Delta \text{PA}}$) are present in each panel. Since the absolute value of PA does not necessarily reflect physical significance, we have not normalized ΔPA by $\text{PA}_{\text{bar,true}}$. It's clear that, regardless of the resolution level, PA_{obs}^n remains consistently close to its intrinsic value. The absolute value of $\overline{\Delta \text{PA}}$ constantly stays less 1 degree. The ΔPA as a function of n can be found in Fig. 11. Our results indicate that resolution has minimal influence on the measurement of the orientation of the bar.

Figure 11 plots the previously discussed change or fractional change ($\Delta \epsilon_{\text{obs}}^n / \epsilon_{\text{bar,true}}$, $\Delta a_{\text{obs}}^n / a_{\text{bar,true}}$, and $\Delta \text{PA}_{\text{obs}}^n$) between parameters measured from low-resolution images generated using the F200W filter and their intrinsic values as a function of resolution ($n = a_{\text{bar,true}}/\text{FWHM}$). These data, along with those obtained using F115W and F150W filters, are listed in Table 1. The dependence of $\Delta \epsilon_{\text{obs}}^n / \epsilon_{\text{bar,true}}$, $\Delta a_{\text{obs}}^n / a_{\text{bar,true}}$, and $\Delta \text{PA}_{\text{obs}}^n$ on n for the F115W or F150W filter are quite similar to those for the F200W filter. However, as has been shown in Fig. 7, the η_{eff} for F115W filter is lower than those for F150W or F120W filter at a given $n > 4$, since the F115W PSF is not Nyquist-sampled at a pixel scale of 0.03 arcsec/pixel. We note that there are fewer than 10 bars identified at $n = 1.44$ and 1.2 for the F115W filter, at $n = 1.2$ for the F150W filter, and at $n = 1$ for the F200W filter, which might influence the statistical significance of the results at these n values.

Table 1. Biases and uncertainties in identifying and quantifying bars in the simulated low-resolution JWST images. Col. (1) resolution level $n = a_{\text{bar, true}}/\text{FWHM}$; (2) averaged value of the fractional difference $\Delta a_{\text{obs}}^n/a_{\text{bar, true}}$, where $\Delta a_{\text{obs}}^n = (a_{\text{obs}}^n - a_{\text{bar, true}})$; (3) standard deviation of $\Delta a_{\text{obs}}^n/a_{\text{bar, true}}$; (4) averaged value of the fractional difference $\Delta \epsilon_{\text{obs}}^n/\epsilon_{\text{bar, true}}$, where $\Delta \epsilon_{\text{obs}}^n = (\epsilon_{\text{obs}}^n - \epsilon_{\text{bar, true}})$; (5) standard deviation of $\Delta \epsilon_{\text{obs}}^n/\epsilon_{\text{bar, true}}$; (6) averaged value of the difference $\Delta \text{PA}_{\text{obs}}^n = \text{PA}_{\text{obs}}^n - \text{PA}_{\text{bar, true}}$; (7) standard deviation of PA_{obs}^n ; (8) effectiveness of detecting bars at specific resolution level.

F115W							
n	$\overline{\Delta a_{\text{obs}}^n}/a_{\text{bar, true}}$	$\sigma_{\Delta a_{\text{obs}}^n}/a_{\text{bar, true}}$	$\overline{\Delta \epsilon_{\text{obs}}^n}/\epsilon_{\text{bar, true}}$	$\sigma_{\Delta \epsilon_{\text{obs}}^n}/\epsilon_{\text{bar, true}}$	$\overline{\Delta \text{PA}_{\text{obs}}^n}$ ($^\circ$)	$\sigma_{\Delta \text{PA}_{\text{obs}}^n}$ ($^\circ$)	η_{eff}
(1)	(2)	(3)	(4)	(5)	(6)	(7)	(8)
10	-0.03	0.08	-0.07	0.06	-0.12	2.58	1.00
5.16	-0.02	0.10	-0.18	0.08	-0.19	3.25	1.00
4.3	-0.02	0.11	-0.22	0.08	-0.16	4.02	0.99
3.58	-0.01	0.12	-0.28	0.10	-0.29	4.70	0.98
2.99	-0.02	0.14	-0.34	0.11	-0.48	5.78	0.89
2.49	-0.02	0.14	-0.40	0.11	-0.51	5.78	0.69
2.07	0.03	0.14	-0.42	0.12	-0.53	6.46	0.35
1.73	0.12	0.17	-0.45	0.14	0.20	5.70	0.11
1.44	0.11	0.00	-0.57	0.02	-8.33	8.92	0.01
1.2	0.00
1	0.00
F150W							
n	$\overline{\Delta a_{\text{obs}}^n}/a_{\text{bar, true}}$	$\sigma_{\Delta a_{\text{obs}}^n}/a_{\text{bar, true}}$	$\overline{\Delta \epsilon_{\text{obs}}^n}/\epsilon_{\text{bar, true}}$	$\sigma_{\Delta \epsilon_{\text{obs}}^n}/\epsilon_{\text{bar, true}}$	$\overline{\Delta \text{PA}_{\text{obs}}^n}$ ($^\circ$)	$\sigma_{\Delta \text{PA}_{\text{obs}}^n}$ ($^\circ$)	η_{eff}
10	-0.02	0.08	-0.04	0.05	-0.18	2.14	1.00
5.16	-0.03	0.10	-0.14	0.08	-0.17	2.46	1.00
4.3	-0.01	0.10	-0.18	0.09	-0.09	3.37	1.00
3.58	-0.02	0.11	-0.23	0.10	-0.13	4.06	0.99
2.99	-0.03	0.13	-0.29	0.10	-0.24	4.64	0.98
2.49	-0.04	0.12	-0.34	0.10	-0.33	4.98	0.94
2.07	-0.01	0.12	-0.39	0.11	-0.39	5.58	0.81
1.73	0.03	0.13	-0.44	0.12	-0.69	6.27	0.53
1.44	0.11	0.16	-0.46	0.11	0.20	7.44	0.17
1.2	0.15	0.14	-0.51	0.12	2.73	5.53	0.02
1	0.00
F200W							
n	$\overline{\Delta a_{\text{obs}}^n}/a_{\text{bar, true}}$	$\sigma_{\Delta a_{\text{obs}}^n}/a_{\text{bar, true}}$	$\overline{\Delta \epsilon_{\text{obs}}^n}/\epsilon_{\text{bar, true}}$	$\sigma_{\Delta \epsilon_{\text{obs}}^n}/\epsilon_{\text{bar, true}}$	$\overline{\Delta \text{PA}_{\text{obs}}^n}$ ($^\circ$)	$\sigma_{\Delta \text{PA}_{\text{obs}}^n}$ ($^\circ$)	η_{eff}
10	-0.01	0.07	-0.02	0.04	0.05	1.70	1.00
5.16	-0.01	0.09	-0.10	0.08	-0.20	2.32	1.00
4.3	-0.02	0.09	-0.15	0.09	-0.25	2.87	1.00
3.58	-0.02	0.12	-0.20	0.10	-0.27	3.79	1.00
2.99	-0.04	0.13	-0.25	0.11	-0.27	4.05	0.99
2.49	-0.06	0.11	-0.30	0.10	-0.34	4.23	0.95
2.07	-0.03	0.10	-0.34	0.10	-0.34	4.90	0.84
1.73	0.02	0.13	-0.40	0.11	-0.43	6.37	0.59
1.44	0.10	0.17	-0.46	0.11	0.25	8.38	0.26
1.2	0.17	0.18	-0.49	0.10	0.98	7.38	0.06
1	0.19	0.15	-0.54	0.08	0.42	6.54	0.03

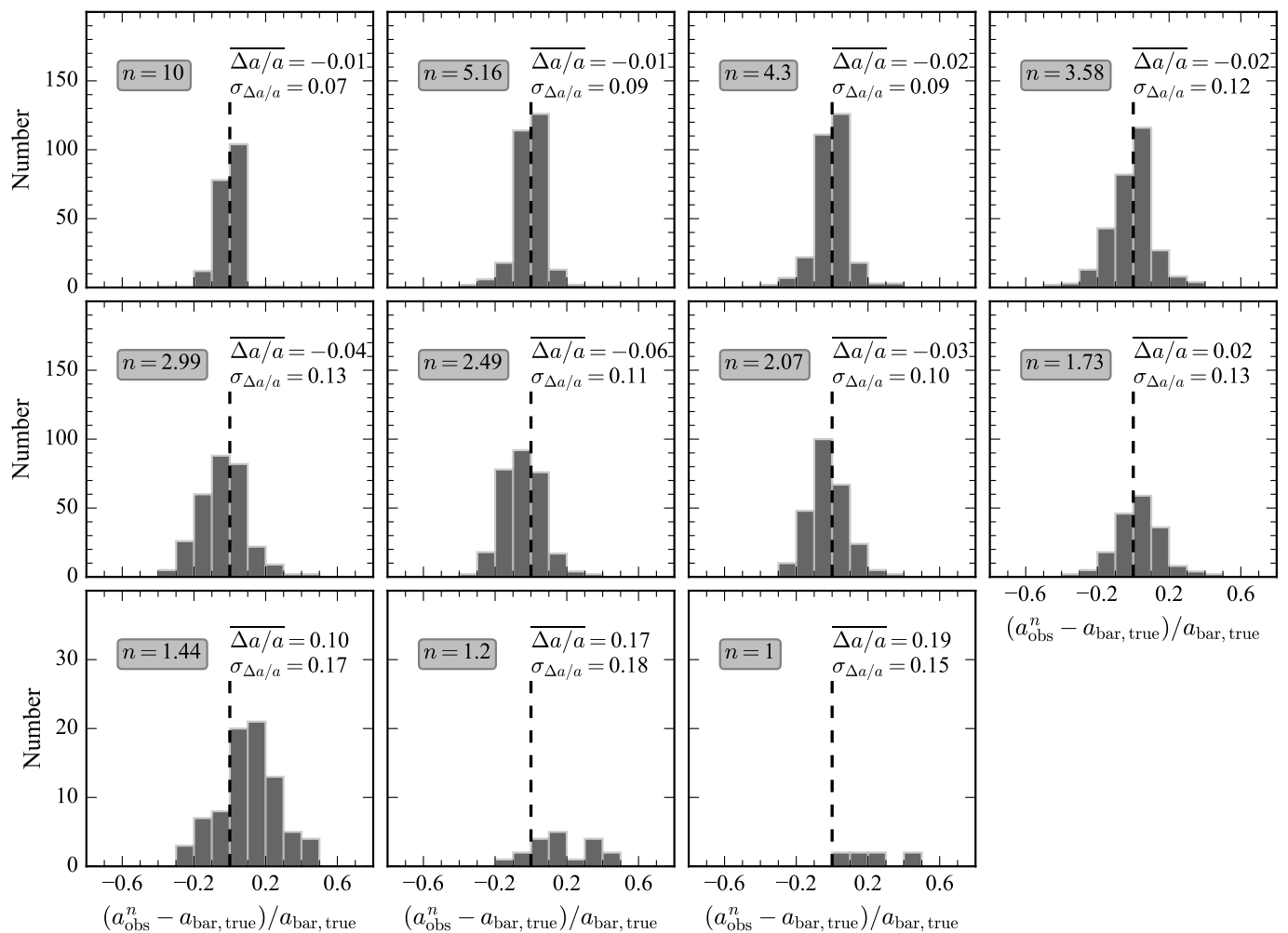


Fig. 8. Distribution of the fractional difference $\Delta a_{\text{obs}}^n / a_{\text{bar, true}}$, where $\Delta a_{\text{obs}}^n = (a_{\text{obs}}^n - a_{\text{bar, true}})$, at various resolution levels $n = a_{\text{bar, true}} / \text{FWHM}$. The $a_{\text{bar, true}}$ denotes the intrinsic value. Results for the F20W PSF are present. The averaged fractional difference ($\overline{\Delta a/a}$) and standard deviation ($\sigma_{\Delta a/a}$) are indicated at the top of each panel. The vertical black dashed line in each panel marks $a_{\text{obs}}^n = a_{\text{bar, true}}$.

4.2. The effect of noise

We investigate the influence of noise on the bar analysis by comparing the parameters ($a_{\text{obs}}^{S/N}$, $\epsilon_{\text{obs}}^{S/N}$, and $\text{PA}_{\text{obs}}^{S/N}$), measured in the simulated low- S/N images, and their noiseless values ($a_{\text{obs}}^{n=4.3}$, $\epsilon_{\text{obs}}^{n=4.3}$, and $\text{PA}_{\text{obs}}^{n=4.3}$), measured in the noiseless low-resolution simulated images of $n = 4.3$. The n is fixed to 4.3 for isolating the effects from noise. As these measurements are relatively robust against noise, we refrain from showing the plots, but list the results in Table 2. This table provides η_{eff} (Eq. [1]), and the mean value ($\overline{\Delta a_{\text{obs}}^{S/N} / a_{\text{obs}}^{n=4.3}}$, $\overline{\Delta \epsilon_{\text{obs}}^{S/N} / \epsilon_{\text{obs}}^{n=4.3}}$, and $\overline{\Delta \text{PA}_{\text{obs}}^{S/N}}$) and standard deviation ($\sigma_{\overline{\Delta a_{\text{obs}}^{S/N} / a_{\text{obs}}^{n=4.3}}}$, $\sigma_{\overline{\Delta \epsilon_{\text{obs}}^{S/N} / \epsilon_{\text{obs}}^{n=4.3}}}$, and $\sigma_{\overline{\Delta \text{PA}_{\text{obs}}^{S/N}}}$) of the change or fractional change of the measured parameters, defined in the same vein as previously did. It can be seen from Table 2 that, when $S/N \geq 11.5$, the η_{eff} remains 100%, suggesting that within this S/N range, all the barred galaxies are able to be detected. As the S/N falls below 11.5, there are a tiny fraction of barred galaxies can be missed. Nevertheless, even though when S/N reaches as low as 3, almost all the bars can be identified. Irrespective of the S/N level, the deviation of the measured $a_{\text{obs}}^{S/N}$, $\epsilon_{\text{obs}}^{S/N}$ and $\text{PA}_{\text{obs}}^{S/N}$ of bars from their noiseless values are quite small, most

of which are $\leq 5\%$ for a , $\leq 1\%$ for ϵ , and ≤ 0.5 degree for PA, though the scatter slightly increase with lower S/N . The above analysis has also been performed for the noiseless simulated images of other values of $a_{\text{bar, true}} / \text{FWHM}$, and the results are almost identical to Table 2. Our results suggest that, under the typical S/N range in CEERS for galaxies with redshifts of $z \leq 3$ and stellar mass of $M_{\star} \geq 10^{9.75} M_{\odot}$, the detection and quantification of bars are not significantly adversely affected by the noise.

In practical applications, it is more straightforward to calculate the effective surface brightness (μ_e), which has similar ability to characterize the clarity of an extended structure similarly to the S/N for a given background noise. To make our results more easily utilized, we compute the mean value of μ_e ($\overline{\mu_e}$) for our simulated images at each S/N level and list them in Table 2. As our simulated images are generated to match the typical noise conditions in the CEERS field, the values of $\overline{\mu_e}$ only work robustly in the CEERS field. These $\overline{\mu_e}$, corresponding to a given S/N , should be fainter in a survey deeper than CEERS but brighter in a shallower survey.

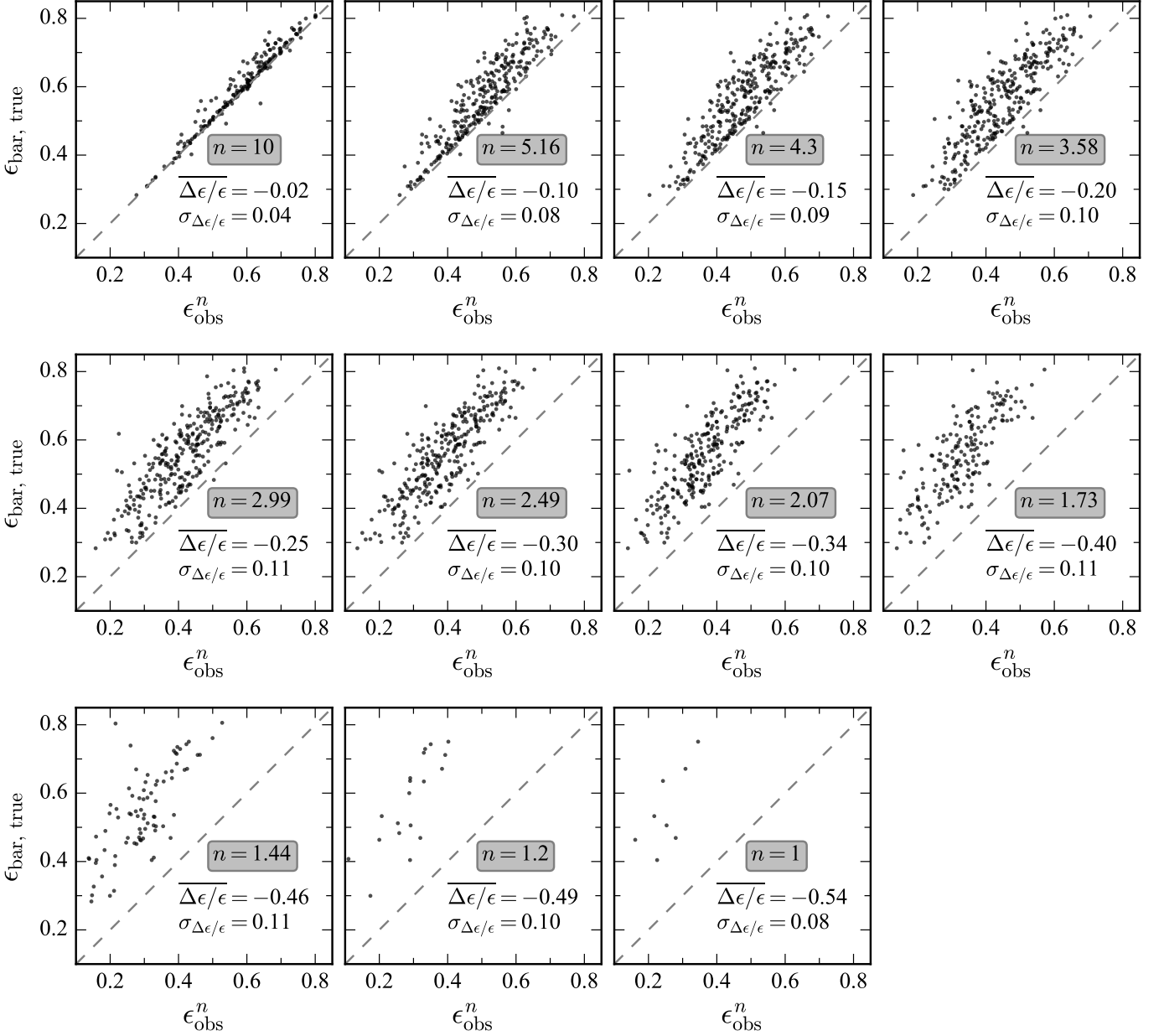


Fig. 9. Comparison between ϵ_{obs}^n and $\epsilon_{\text{bar,true}}$ at each resolution level $n = a_{\text{bar,true}}/\text{FWHM}$. Results for the F200W filter are present. The fractional difference between ϵ_{obs}^n and $\epsilon_{\text{bar,true}}$ is denoted as $\Delta\epsilon/\epsilon = (\epsilon_{\text{obs}}^n - \epsilon_{\text{bar,true}})/\epsilon_{\text{bar,true}}$. The mean value ($\overline{\Delta\epsilon/\epsilon}$) and standard deviation ($\sigma_{\Delta\epsilon/\epsilon}$) of the fractional difference are indicated in each panel. The one-to-one relation is displayed by a dashed line.

4.3. Bar identification and measurement in simulated CEERS images

In this section, we explore how the identification and quantification of bars at high redshifts are influenced by the combination of observational effects and evolution effects using the simulated CEERS images with galaxy evolution models included. The dependence of method effectiveness of detecting bars (η_{eff} ; on the left y-axis) and observed bar fraction ($f_{\text{bar,obs}}$; on the right y-axis) on redshift z are shown by the grey diamonds in Fig. 12. The error bars associated with the data points are the uncertainty of $f_{\text{bar,obs}}$. The $f_{\text{bar,obs}}$ is defined as the ratio of number of bars identified at each redshift to the total number of disk galaxies:

$$f_{\text{bar,obs}} = \frac{\text{Number of detected bars}}{\text{Number of disks}}. \quad (2)$$

As redshift increases from 0 to 3, the η_{eff} exhibits a gradual decrease, declining from 100% to approximately 55%, suggesting more and more bars being missing at higher redshifts due to the impact of observational effects. Approximately half of the bars can go undetected at $z = 3$. Meanwhile, the $f_{\text{bar,obs}}$ decreases from 68% to 37.5%, suggesting that the bar fraction observed at JWST F200W band can be underestimated by 30% at $z = 3$ compared to local universe. The $\eta_{\text{eff}}-z$ and $f_{\text{bar,obs}}-z$ relations are not smooth but present two sudden declines at $z = 1.0$ and $z = 1.75$, which stems from the changes of the filters. From $z = 1.0$ to $z = 1.25$, for better tracing the rest-frame optical light, the F115W is changed to F150W, the image PSFs broadens, causing the images to become blurrier and thus reducing the bar detection capability. When the F150W filter is changed

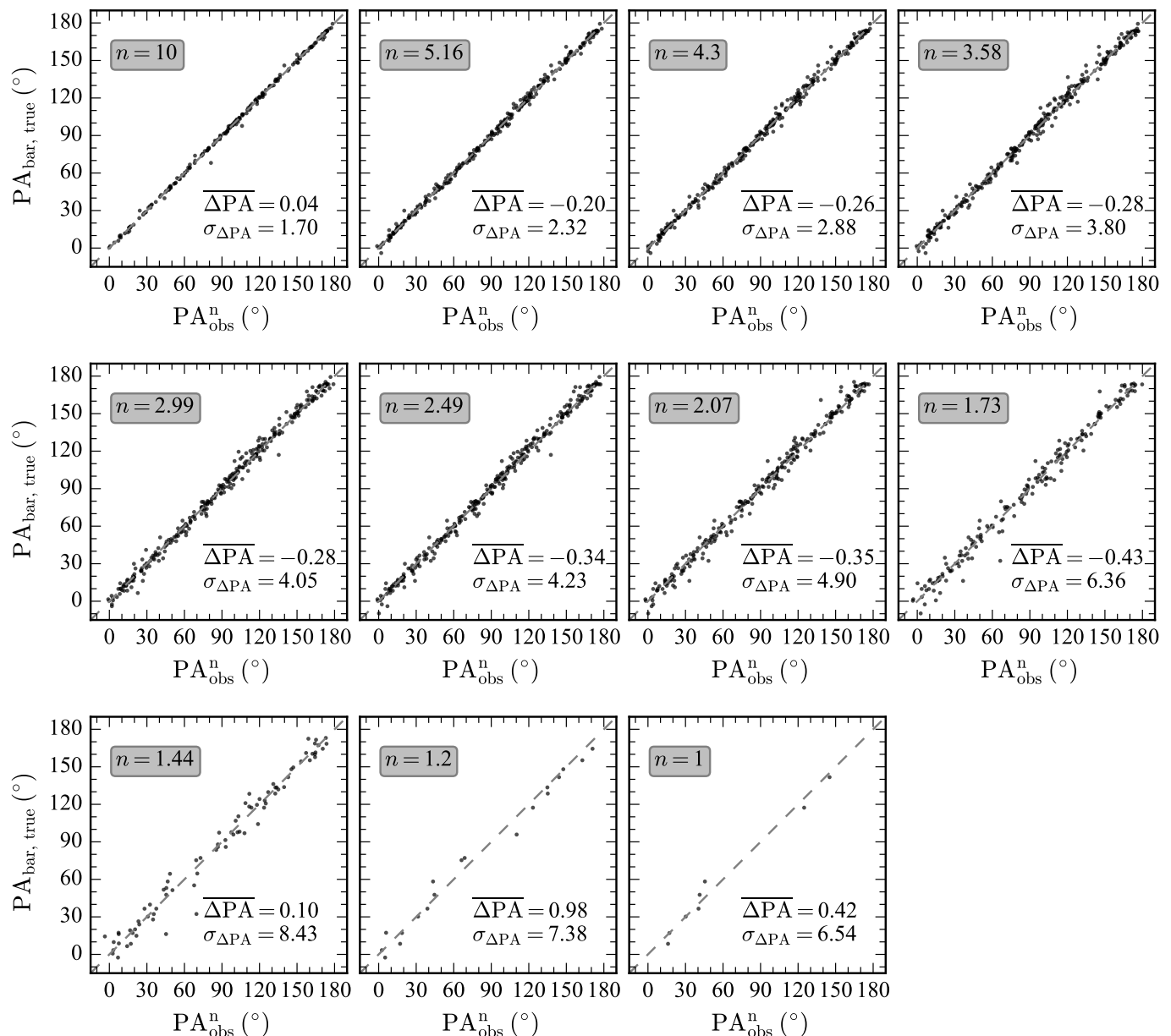


Fig. 10. Comparison between PA_{obs}^n and $PA_{\text{bar, true}}$ at each resolution level $n = a_{\text{bar, true}}/\text{FWHM}$. Results for the F200W filter are present. The difference between PA_{obs}^n and $PA_{\text{bar, true}}$ is denoted as $\Delta PA = PA_{\text{obs}}^n - PA_{\text{bar, true}}$. The mean difference ($\overline{\Delta PA}$) and standard deviation ($\sigma_{\Delta PA}$) are indicated in each panel. The one-to-one relation is displayed by a dashed line.

to F200W at $z = 2.0$, the same principle applies. The trend of decreasing of apparent $f_{\text{bar, obs}}$ with increasing z is consistent with Erwin (2018), who used S⁴G images to simulate the resolution of high-redshift HST images and generated a decreasing trend of bar fraction toward higher redshifts by applying a cut in bar size to select barred galaxies.

For comparison, we shown the results for the simulated images without involving galaxies evolutions as pink stars in Fig. 12. The measured $f_{\text{bar, obs}}$ at $z \leq 1.25$ is almost identical to the results from the simulated CEERS image with involving galaxies evolutions. However, as redshift increases, the $f_{\text{bar, obs}}$ decreases significantly, reaching 11% at $z = 3.0$. This decrease is caused by the S/N being too low due to the cosmological dimming effect, as discussed in Sect. 3.

In Fig. 13, we plot the fractional difference ($\Delta a_{\text{obs}}^z/a_{\text{bar, true}}$, $\Delta \epsilon_{\text{obs}}^z/\epsilon_{\text{bar, true}}$) or absolute difference (ΔPA_{obs}^z) between the three parameters measured from the simulated CEERS images at each redshift and their intrinsic values. As shown in the top row, the $\Delta a_{\text{obs}}^z/a_{\text{bar, true}}$ at each redshift is slightly less than zero on average, suggesting that the bar size measurements at higher redshifts are relatively robust, with only a few percent underestimation ($\leq 4\%$) to be noted. The relation between $\Delta a_{\text{obs}}^z/a_{\text{bar, true}}$ and z does not reveal the systematic overestimation in measured bar size when resolution is very low as might be expected from Fig. 11. This is because most short bars with size $a_{\text{bar, true}} \lesssim 2 \times \text{FWHM}$ have been missed (Fig. 7) in the process of bar identification for the simulated CEERS images. Specifically, at $z = 3$, there are 90% of identified bars with size $a_{\text{bar, true}} > 2 \times \text{FWHM}$, therefore leading to a minor underestimation of measured bar

Table 2. Biases and uncertainties in identifying and quantifying bars in the simulated low- S/N JWST images. Col. (1) different S/N level; (2) averaged value of the fractional difference $\Delta a_{\text{obs}}^{S/N}/a_{\text{obs}}^{n=4.3}$, where $\Delta a_{\text{obs}}^{S/N} = (a_{\text{obs}}^{S/N} - a_{\text{obs}}^{n=4.3})$; (3) Standard deviation of $\Delta a_{\text{obs}}^{S/N}/a_{\text{obs}}^{n=4.3}$; (4) averaged value of the fractional difference $\Delta \epsilon_{\text{obs}}^{S/N}/\epsilon_{\text{obs}}^{n=4.3}$, where $\Delta \epsilon_{\text{obs}}^{S/N} = (\epsilon_{\text{obs}}^{S/N} - \epsilon_{\text{obs}}^{n=4.3})$; (5) standard deviation of $\Delta \epsilon_{\text{obs}}^{S/N}/\epsilon_{\text{obs}}^{n=4.3}$; (6) averaged value of the difference $\Delta \text{PA}_{\text{obs}}^{S/N} = \text{PA}_{\text{obs}}^{S/N} - \text{PA}_{\text{obs}}^{n=4.3}$; (7) standard deviation of $\text{PA}_{\text{obs}}^{S/N}$; (8) effectiveness of detecting bars at specific S/N level; (9) the effective surface brightness μ_e .

S/N	$\overline{\Delta a_{\text{obs}}^{S/N}/a_{\text{obs}}^{n=4.3}}$	$\sigma_{\Delta a_{\text{obs}}^{S/N}/a_{\text{obs}}^{n=4.3}}$	$\overline{\Delta \epsilon_{\text{obs}}^{S/N}/\epsilon_{\text{obs}}^{n=4.3}}$	$\sigma_{\Delta \epsilon_{\text{obs}}^{S/N}/\epsilon_{\text{obs}}^{n=4.3}}$	$\overline{\Delta \text{PA}_{\text{obs}}^{S/N}}$	$\sigma_{\Delta \text{PA}_{\text{obs}}^{S/N}}$	η_{eff}	$\overline{\mu_e}$
(1)	(2)	(3)	(4)	(5)	(6)	(7)	(8)	(9)
					($^\circ$)	($^\circ$)		(mag arcsec $^{-2}$)
62	0.00	0.02	0.00	0.05	-0.02	0.02	1.00	18.96
44.3	0.00	0.02	0.00	0.05	0.05	0.02	1.00	19.64
31.6	0.00	0.02	0.00	0.05	0.03	0.02	1.00	20.30
22.6	0.00	0.03	0.00	0.05	-0.08	0.03	1.00	20.92
16.1	0.00	0.02	0.01	0.05	0.04	0.02	1.00	21.51
11.5	0.01	0.04	0.00	0.06	-0.01	0.04	1.00	22.06
8.2	0.01	0.03	0.01	0.06	-0.01	0.03	1.00	22.57
5.9	0.02	0.05	0.01	0.07	-0.15	0.05	0.99	23.04
4.2	0.03	0.05	0.01	0.08	-0.05	0.05	0.99	23.50
3	0.04	0.06	0.01	0.09	-0.46	0.06	0.96	23.93

size according to Fig. 11. The relation between $\Delta \epsilon_{\text{obs}}^z/\epsilon_{\text{bar, true}}$ and z shows that the measured bar ellipticities are on average more and more underestimated at redshift increasing from $z = 0.75$ to $z = 2.0$, but the underestimation become approximately constant beyond $z = 2.0$. One might think that, as galaxies become angularly smaller at high redshifts, the $\Delta \epsilon_{\text{obs}}^z/\epsilon_{\text{bar, true}}$ should decrease strictly monotonically with higher z according to Fig. 11, but this conjecture is not true. The decline in $\Delta \epsilon_{\text{obs}}^z/\epsilon_{\text{bar, true}}$ from $z = 0.75$ to $z = 2$ is indeed due to the significant reduction in the angular size of galaxies, in which effects from longer distance and size evolution of the disks are considered. However, at higher redshifts, more and more bars become angularly too small to be detected, so that the contribution of severely underestimation in ϵ caused by short bars to the calculation of mean value is significantly reduced, leading to a approximate constant average $\Delta \epsilon_{\text{obs}}^z/\epsilon_{\text{bar, true}}$ between $z = 2$ and $z = 3$. As expected, the measurement of PA is quite robust without any obvious systematic biases.

4.4. Correction of the measurement biases

While the PA measurement remains unbiased, the measurements of a and ϵ are biased towards lower values at high redshifts, with resolution effects being the primary cause. With the fractional differences between the measurements from the low-resolution images and their intrinsic values listed in Table 1, we can effectively remove the biases introduced by resolution. The biased-corrected bar size, denoted by a_{cor}^z , can be obtained through

$$a_{\text{cor}}^z = \frac{a_{\text{obs}}^z}{(\Delta a_{\text{obs}}^n/a_{\text{bar, true}} + 1)}, \quad (3)$$

where n is approximated as $a_{\text{obs}}^z/\text{FWHM}$ and the value of $\Delta a_{\text{obs}}^n/a_{\text{bar, true}}$ is obtained via interpolation based on the data in Table 1. The same methodology can be applied to obtain the

biased-corrected bar ellipticity, denoted as ϵ_{cor}^z :

$$\epsilon_{\text{cor}}^z = \frac{\epsilon_{\text{obs}}^z}{(\Delta \epsilon_{\text{obs}}^n/\epsilon_{\text{bar, true}} + 1)}, \quad (4)$$

where the value of $\Delta \epsilon_{\text{obs}}^n/\epsilon_{\text{bar, true}}$ is obtained through interpolation. Figure 14 plots the fractional difference ($\Delta a_{\text{cor}}^z/a_{\text{bar, true}}$) between a_{cor}^z and its intrinsic value $a_{\text{bar, true}}$ in the top panel and the fractional difference ($\Delta \epsilon_{\text{cor}}^z/\epsilon_{\text{bar, true}}$) between ϵ_{cor}^z and its intrinsic value $\epsilon_{\text{bar, true}}$ in the bottom panel. After making corrections, the values of a_{cor}^z and ϵ_{cor}^z underestimate $a_{\text{bar, true}}$ and $\epsilon_{\text{bar, true}}$ by less than 1% on average. The residuals are negligibly small, indicating that our correction functions are effective.

5. Implication

Determining the bar fraction at high redshifts is crucial to understand the nature of bars, but it is challenging due to band shifting and/or image degradation (Sheth et al. 2008). Early HST-based study of the bar fraction evolution reported a significant decrease beyond $z \sim 0.5$ (Abraham et al. 1999). Then Sheth et al. (2003) found that the fraction of strong bars at $z > 0.7$ (4/95) is higher than the fraction observed at $z < 0.7$ (1/44). These fractions are likely lower limits, primarily due to resolution effects and the small-number statistic. With the images of improved resolution obtained from the HST Advanced Camera for Surveys (ACS), two subsequent studies of Elmegreen et al. (2004) and Jogee et al. (2004) reported a relatively consistent fraction up to redshifts $z \sim 1$. Nevertheless, their samples are still of a modest size. With a statistical large sample of more than 2000 galaxies defined from the Cosmic Evolution Survey (COSMOS; Scoville et al. 2007), Sheth et al. (2008) showed that the bar fraction declines from $\sim 65\%$ in the local universe to $\sim 20\%$ at $z \approx 0.84$. Although the overall bar fractions calculated based on Galaxy Zoo have been underestimated (Erwin 2018), studies based on it have consistently identified a trend declining from $\sim 22\%$ at $z = 0.4$ to $\sim 11\%$ at $z = 1.0$ (Melvin et al. 2014).

Table 3. Summary of bar fractions measured from simulated CEERS images at different redshifts using different methods. Col. (1) redshift; (2) the bar fraction ($f_{\text{bar, obs}}$) measured from simulated CEERS images using the ellipse fitting method as described in Sect 2; (3)–(6) the $f_{\text{bar, obs}}$ estimated from simulated CEERS images by adopting the cut of $a_{\text{bar, true}} > 2 \times \text{FWHM}$ for bar detection for four different NIRcam filters.

z	$f_{\text{bar, obs}}(\text{ellipse})$	$f_{\text{bar, obs}}^{\text{F200W}}(\text{cut})$	$f_{\text{bar, obs}}^{\text{F277W}}(\text{cut})$	$f_{\text{bar, obs}}^{\text{F356W}}(\text{cut})$	$f_{\text{bar, obs}}^{\text{F444W}}(\text{cut})$
(1)	(2)	(3)	(4)	(5)	(6)
0.0	0.68	0.68	0.68	0.68	0.68
0.75	0.62	0.55	0.46	0.36	0.27
1.0	0.58	0.51	0.40	0.29	0.19
1.25	0.52	0.47	0.35	0.23	0.15
1.5	0.50	0.45	0.32	0.19	0.13
1.75	0.47	0.42	0.29	0.17	0.10
2.0	0.42	0.40	0.27	0.15	0.08
2.25	0.40	0.39	0.25	0.15	0.08
2.5	0.39	0.38	0.23	0.14	0.06
2.75	0.38	0.37	0.22	0.13	0.06
3.0	0.38	0.37	0.21	0.12	0.06

Previous studies have consistently raised concerns about the possibility of missing short bars at higher redshifts due to resolution limitations. Lacking rigorous quantitative justification, Sheth et al. (2003) proposed a bar size threshold of 2.5 times the PSF FWHM for bar detection. Concluding from experiments on artificial galaxies, Aguerri et al. (2009) proposed the same the threshold. Erwin (2018) suggested a smaller threshold of 2 times the PSF FWHM. In Fig. 7, we demonstrate that, for images with a Nyquist-sampling PSF, the effectiveness of detecting bars η_{eff} remains at $\sim 100\%$ when $a_{\text{bar, true}}/\text{FWHM}$ is above 2. When $a_{\text{bar, true}}/\text{FWHM}$ is below 2, the η_{eff} declines sharply. We select the bars in the simulated CEERS images using criterion $a_{\text{bar, true}} > \text{F200W FWHM}$, calculate the $f_{\text{bar, obs}}$, and plot them as pink square in Fig. 15. These $f_{\text{bar, obs}}$ are fully consistent with the F200W-band $f_{\text{bar, obs}}$ derived from the ellipse fitting method, which are represented as grey diamonds in the plot. This suggests that using $a_{\text{bar, true}} = 2 \times \text{FWHM}$ as the bar detection threshold provides a better fit to the results obtained through the ellipse fitting method. Using the factor of 2.5 would underestimate the bar-detection efficiency of the ellipse fitting method. Nevertheless, if the PSFs are not Nyquist-sampling, the effectiveness of detecting bars starts to decline at higher $a_{\text{bar, true}}/\text{FWHM}$, suggesting a higher bar size threshold. The concern of missing bars due to resolution effects is further amplified by the growth of bar size over cosmic time, as indicated by simulation studies (e.g., Debattista & Sellwood 2000; Martinez-Valpuesta et al. 2006; Agorri et al. 2017; Rosas-Guevara et al. 2022).

Meanwhile, studies on bars based on cosmological simulations also highlight the potential impacts rising from resolution effects. By studying TNG100 galaxies, Zhao et al. (2020) revealed a roughly constant bar fraction of $\sim 60\%$ at $0 < z < 1$ when selecting galaxies with a mass cut of $M_{\star} \geq 10^{10.6} M_{\odot}$. However, considering the resolution limitations observed in HST images, where bars shorter than 2 kpc can be missed at $z \sim 1$, they focus on bars longer than 2.2 kpc and consequently detect a decreasing trend of bar fraction at higher redshifts. Moreover, Rosas-Guevara et al. (2022) used the data from TNG50 to study spiral galaxies with $M_{\star} \geq 10^{10} M_{\odot}$, showing that the derived bar fraction increases from 28% at $z = 4$, and reaches a peak of 48% at $z = 1$ and then drops to 30% at $z = 0$. Considering the

$2 \times \text{FWHM}$ detection limit, they implemented an angular resolution limit equivalent to twice the HST F814W PSF FWHM. As a result, the bar fraction exhibited a decrease with increasing redshift at $z > 0.5$, which relatively reconciles the differences between their results and observations.

With the advent of JWST, obtaining deep high-resolution NIR images has become accessible, enabling us to explore the structures in high-redshift galaxies in detail. Recently, Guo et al. (2023) analyse rest-frame NIR galaxy structures using F444W images from JWST CEERS and report the detection of six strongly barred galaxies at $1 < z < 3$.

Costantin et al. (2023) remarkably reported a barred galaxy at $z \approx 3$ from CEERS, making it the most distant barred galaxy ever detected. This discovery suggests that dynamically cold disk galaxies could have already been in place at $z = 4$ –5. Our findings, derived from simulated CEERS data, can serve as a comparison sample for studies of high-redshift bar fraction based on JWST. Grey diamonds in Figure 15 plots the observed $f_{\text{bar, obs}}$ from the simulated CEERS images in the F115W band for $z = 0.75$ –1.0, F150W band for $z = 1.25$ –1.75, and F200W band for $z = 2.0$ –3.0. We restate that the CEERS image simulation procedure incorporates the changes in angular size due to both distance and the intrinsic evolution of disk size. As a result, bars in the simulated CEERS images appear shorter in physical size at higher redshift, directly following the disk size evolution described by van der Wel et al. (2014). Specifically, at redshifts $z = 1$, $z = 2$, and $z = 3$, bars are approximately 63%, 48%, and 40% the size of their local counterparts. In contrast, the ratio of the bar size to disk size remains unchanged, and the true bar fraction is fixed to 68%, the value measured in DESI images (Sect. 2). To present the results based on other long-wavelength NIRcam filters (F277W, F356W, and F444W), we estimate the measured $f_{\text{bar, obs}}$ using the current simulated dataset by adopting the criterion of $a_{\text{bar, true}} > 2 \times \text{FWHM}$ for bar detection, as proposed by Erwin (2018). First, we apply $a_{\text{bar, true}} > 2 \times \text{F200W FWHM}$ to detect bars, calculate $f_{\text{bar, obs}}$ observed in the F200W band, and plot them as pink squares in Fig. 15. They are in good agreement with the results at redshift $2 \leq z \leq 3$ obtained from the ellipse fitting method, demonstrating the effectiveness of the $a_{\text{bar, true}} > 2 \times \text{F200W FWHM}$ crite-

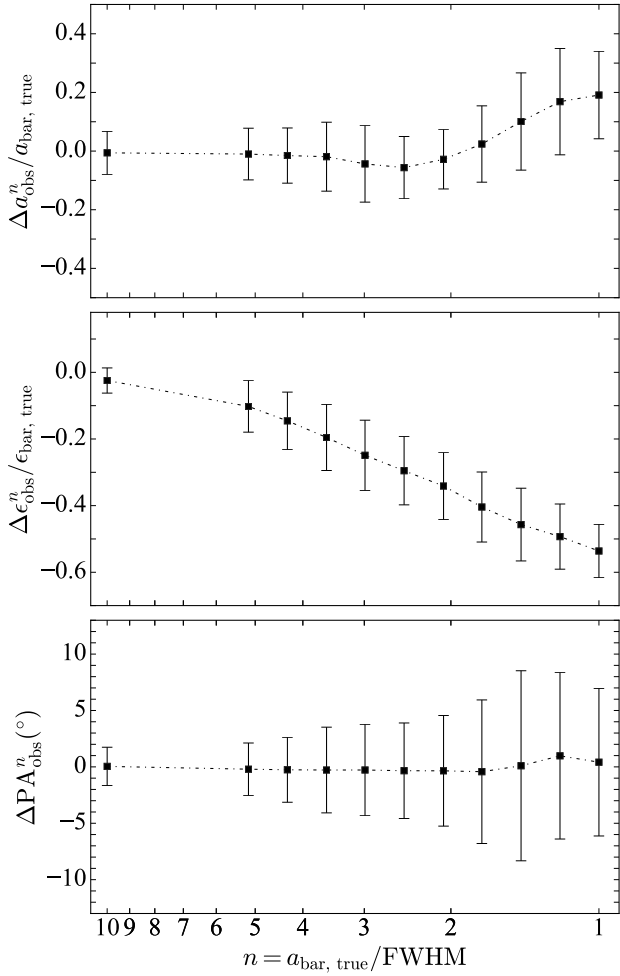


Fig. 11. Change or fractional change between measure parameters and their intrinsic values as a function of resolution $n = a_{\text{bar, true}}/\text{FWHM}$. Results for the F200W filter are present.

rior. Subsequently, using $a_{\text{bar, true}} > 2 \times \text{F277W FWHM}$, we calculate the F277W-band $f_{\text{bar, obs}}$ observed in the simulated CEERS images, and plot them as green stars. The observed $f_{\text{bar, obs}}$ in the F277W band is lower than its F200W-band counterpart because the F277W PSF FWHM is larger than the F200W PSF FWHM. The same calculations are applied to the F356W and F444W bands. We summarize the measured values of $f_{\text{bar, obs}}$ as a function of redshifts for the four NIRcam bands in Table 3.

We note that the F444W-band $f_{\text{bar, obs}}$ decreases significantly from 68% at $z \approx 0$ to 13% at $z = 1.5$, and further to 6% at $z = 3.0$. We plot the F444W-band bar fraction observed in JWST CEERS and the Public Release Imaging for Extragalactic Research (PRIMER; Dunlop et al. 2021) measured by Le Conte et al. (2024) as black triangles in Fig. 15. The F444W-band $f_{\text{bar, obs}}$ from the simulated CEERS images is consistent within 1σ uncertainty with those obtained from JWST F444W-band observations reported in Le Conte et al. (2024), despite potential difference in the sample properties. Therefore, by accounting for resolution effects and bar size evolution, we have successfully largely reproduced the bar fraction observed by JWST in the F444W band without including evolution of intrinsic bar fraction. Our findings are consistent with Erwin (2018), who similarly factored in resolution effects and assumed bar sizes to be half their actual values at high redshifts. Using S⁴G images

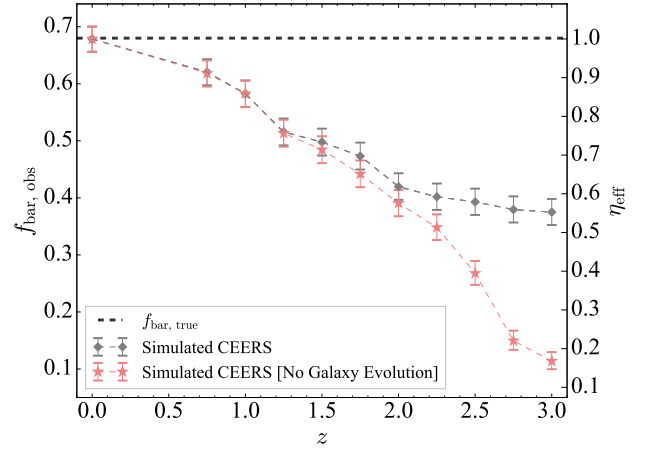


Fig. 12. Dependence of fraction of bars ($f_{\text{bar, obs}}$) and effectiveness of detecting bars (η_{eff}), measured from the simulated CEERS images, as a function of redshift (z). The grey diamonds represent the results obtained from the simulated data with the galaxy evolution model, while the pink stars represent those from the data without. Error bars denote the uncertainty of $f_{\text{bar, obs}}$. For the simulated CEERS images, the F115W, F150W, and F200W filters are used for redshift range $z = 0.75\text{--}1.0$, $1.25\text{--}1.75$, and $2.0\text{--}3.0$, respectively. The horizontal dashed line represents the $f_{\text{bar, true}}$ of 68% of our sample.

for simulated observations, they reproduced the relation between observed bar fraction and stellar mass at redshifts up to 0.84, as reported by Sheth et al. (2008). Our results imply that by positing the presence of all local bars as early as $z \sim 3$, the combination of resolution effects and bar size growth can largely account for the apparent redshift evolution in observed bar fraction found by Le Conte et al. (2024). Any intrinsic evolution in bar fraction, if it exists, might be artificially exaggerated by these factors. To truly grasp the evolution of intrinsic bar fraction, it's imperative to disentangle it from resolution effects and bar size evolution.

6. Conclusions

Quantifying the evolution of bar fraction and bar properties is essential for understanding the evolutionary history of disk galaxies. During the HST era, a series of studies have extensively explored this subject (e.g., Elmegreen et al. 2004; Jogee et al. 2004; Sheth et al. 2008; Pérez et al. 2012; Melvin et al. 2014; Kim et al. 2021). However, these results are potentially affected by limitations of image quality. Nowadays, with the superior high-resolution and deep NIR imaging available from JWST, bars in galaxies at high redshift can be studied in far more detail and some bars at $z > 2$ have been successfully detected (Guo et al. 2023; Le Conte et al. 2024). But still, the difficulties caused by limited observations are unavoidable, making it challenging to fully embrace the intrinsic results. To assess our ability to analyze bars in high-redshift galaxies observed by JWST, we use a sample of 448 nearby face-on spiral galaxies, a subset of the sample conducted by Yu et al. (2023), to simulate images under various observational conditions consistent with the JWST CEERS field, identify bars and quantify bar properties, and then compare the results before and after simulation to determine the systematic biases arising from resolution, noise, or the combination of both. The intrinsic bar size is denoted as $a_{\text{bar, true}}$. The ratio $a_{\text{bar, true}}/\text{FWHM}$ is used to gauge the detectability of bars. Our main findings can be summarized as follows:

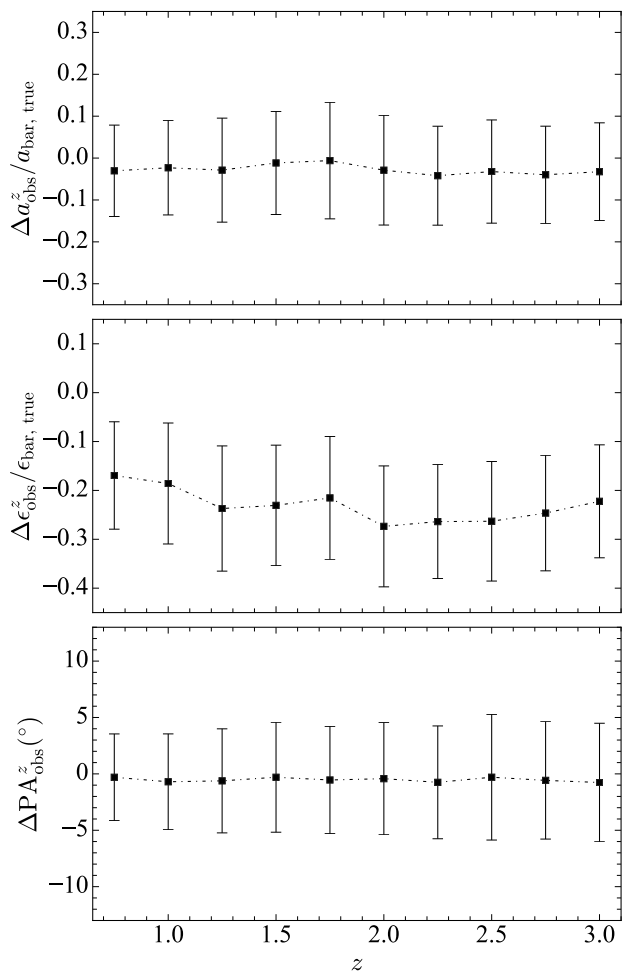


Fig. 13. Fractional difference ($\Delta a_{\text{obs}}^z/a_{\text{bar,true}}$ and $\Delta \epsilon_{\text{obs}}^z/\epsilon_{\text{bar,true}}$) or absolute difference ($\Delta \text{PA}_{\text{obs}}^z$) between parameters measured from the simulated CEERS images and their intrinsic values plotted against redshift (z). The error bar represents the standard deviation of the results at each redshift.

1. Both the identification and quantification of bars are hardly affected by noise when the S/N is greater than 3, an observational condition met by CEERS galaxies with $M_{\star} \geq 10^{9.75} M_{\odot}$ at $z < 3$.
2. For the F200W PSF, which is Nyquist-sampled, the effectiveness of detecting bars remains at ~ 1 when $a_{\text{bar,true}}/\text{FWHM}$ is above a critical value of 2; when $a_{\text{bar,true}}/\text{FWHM}$ is below 2, the effectiveness drops sharply. The fractions of bars determined through ellipse fitting method is in good agreement with that derived using the criterion $a_{\text{bar,true}} > 2 \times \text{FWHM}$, a bar size threshold suggested by Erwin (2018) for bar detection. Nevertheless, when the PSF is sub-Nyquist-sampled, the critical $a_{\text{bar,true}}/\text{FWHM}$ increases. For instance, For the F115W PSF at a pixel scale of 0.03 arcsec/pixel, this critical value is ~ 3 .
3. By assuming all local bars were already in place at high redshifts, we show that a combination of resolution effects and bar size growth can explain the apparent evolution of bar fraction obtained from JWST observations reported by Le Conte et al. (2024). This implies that the reported bar fraction has been significantly underestimated. The

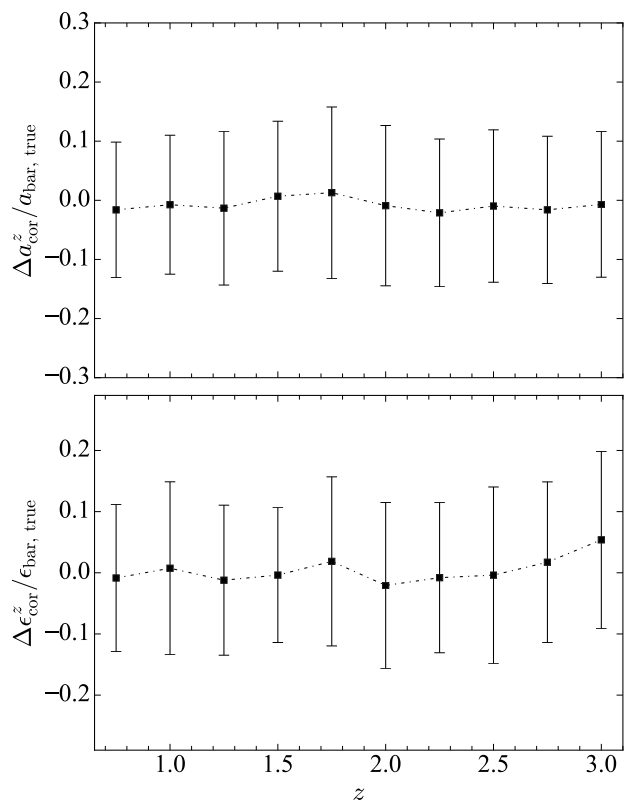


Fig. 14. Fractional difference ($\Delta a_{\text{cor}}^z/a_{\text{bar,true}}$ and $\Delta \epsilon_{\text{cor}}^z/\epsilon_{\text{bar,true}}$) between bias-corrected parameters measured from the simulated CEERS images and their intrinsic values plotted against the redshift (z). The error bar represents the standard deviation of the results at a given redshift.

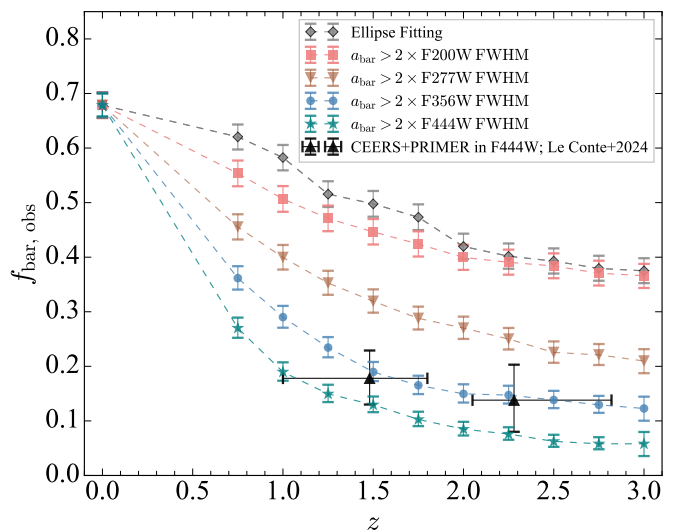


Fig. 15. The measured bar fraction ($f_{\text{bar,obs}}$) obtained from simulated CEERS images as a function of redshifts (z). The grey diamonds represent the $f_{\text{bar,obs}}$ obtained using the ellipse fitting method for simulated CEERS images. The other symbols mark the results obtained by adopting the criterion of $a_{\text{bar,true}} > 2 \times \text{FWHM}$ for bar detection for specific JWST NIRcam filters. The pink rectangles, brown inverted triangles, blue dots, and green stars represent the $f_{\text{bar,obs}}$ for F200W, F277W, F356W, and F444W filter, respectively. Black triangles correspond to the observed F444W-band bar fraction measured by Le Conte et al. (2024).

true bar fraction evolution, if it exists, could be shallower than detected. Our results underscores the importance of disentangling the true bar fraction evolution from resolution effects and bar size growth.

- The measured bar size and bar ellipticity are typically underestimated, with the extent depending on $a_{\text{bar, true}}/\text{FWHM}$. In contrast, the measurement of the bar position angle remains unaffected by resolution. To remove these resolution effects, we have developed correction functions. When applied to the bar properties measured from the simulated CEERS images of high-redshift galaxies, these corrections yield bias-corrected values closely matching their intrinsic values.

Acknowledgements. This work was supported by the National Science Foundation of China (11721303, 11890692, 11991052, 12011540375, 12133008, 12221003, 12233001), the National Key R&D Program of China (2017YFA0402600, 2022YFF0503401), and the China Manned Space Project (CMS-CSST-2021-A04, CMS-CSST-2021-A06). We thank the referee for his insightful and constructive feedback, which significantly enhanced the quality and clarity of this letter. SY acknowledges the support by the Alexander von Humboldt Foundation. Kavli IPMU is supported by World Premier International Research Center Initiative (WPI), MEXT, Japan

References

- Abraham, R. G., Merrifield, M. R., Ellis, R. S., Tanvir, N. R., & Brinchmann, J. 1999, *MNRAS*, 308, 569
- Abraham, R. G., Tanvir, N. R., Santiago, B. X., et al. 1996, *MNRAS*, 279, L47
- Aguerri, J. A. L., Beckman, J. E., & Prieto, M. 1998, *AJ*, 116, 2136
- Aguerri, J. A. L., Méndez-Abreu, J., & Corsini, E. M. 2009, *A&A*, 495, 491
- Algorry, D. G., Navarro, J. F., Abadi, M. G., et al. 2017, *MNRAS*, 469, 1054
- Anderson, S. R., Gough-Kelly, S., Debattista, V. P., et al. 2024, *MNRAS*, 527, 2919
- Athanassoula, E. 1992, *MNRAS*, 259, 345
- Athanassoula, E. 2002, *ApJ*, 569, L83
- Athanassoula, E. 2013, in *Secular Evolution of Galaxies*, ed. J. Falcón-Barroso & J. H. Knapen, 305
- Athanassoula, E., Lambert, J. C., & Dehnen, W. 2005, *MNRAS*, 363, 496
- Athanassoula, E. & Misiriotis, A. 2002, *MNRAS*, 330, 35
- Bagley, M. B., Finkelstein, S. L., Koekemoer, A. M., et al. 2023, *ApJ*, 946, L12
- Barazza, F. D., Jogee, S., & Marinova, I. 2008, *ApJ*, 675, 1194
- Barbary, K. 2016, *Journal of Open Source Software*, 1, 58
- Barden, M., Rix, H.-W., Somerville, R. S., et al. 2005, *ApJ*, 635, 959
- Bertin, E. & Arnouts, S. 1996, *A&AS*, 117, 393
- Buta, R., Laurikainen, E., Salo, H., & Knapen, J. H. 2010, *ApJ*, 721, 259
- Buta, R. J., Sheth, K., Athanassoula, E., et al. 2015, *ApJS*, 217, 32
- Cameron, E., Carollo, C. M., Oesch, P., et al. 2010, *MNRAS*, 409, 346
- Cavanagh, M. K., Bekki, K., & Groves, B. A. 2023, *MNRAS*, 520, 5885
- Conselice, C. J., Rajgor, S., & Myers, R. 2008, *MNRAS*, 386, 909
- Costantin, L., Pérez-González, P. G., Guo, Y., et al. 2023, *Nature*, 623, 499
- de Vaucouleurs, G., de Vaucouleurs, A., Corwin, Herold G., J., et al. 1991, *Third Reference Catalogue of Bright Galaxies*
- Debattista, V. P. & Sellwood, J. A. 2000, *ApJ*, 543, 704
- Desai, V., Dalcanton, J. J., Aragón-Salamanca, A., et al. 2007, *ApJ*, 660, 1151
- Dey, A., Schlegel, D. J., Lang, D., et al. 2019, *AJ*, 157, 168
- Díaz-García, S., Salo, H., Laurikainen, E., & Herrera-Endoqui, M. 2016, *A&A*, 587, A160
- Dunlop, J. S., Abraham, R. G., Ashby, M. L. N., et al. 2021, *PRIMER: Public Release IMaging for Extragalactic Research, JWST Proposal. Cycle 1, ID. #1837*
- Ellison, S. L., Nair, P., Patton, D. R., et al. 2011, *MNRAS*, 416, 2182
- Elmegreen, B. G. & Elmegreen, D. M. 1985, *ApJ*, 288, 438
- Elmegreen, B. G., Elmegreen, D. M., & Hirst, A. C. 2004, *ApJ*, 612, 191
- Elmegreen, B. G., Elmegreen, D. M., Knapen, J. H., et al. 2007, *ApJ*, 670, L97
- Erwin, P. 2005, *MNRAS*, 364, 283
- Erwin, P. 2018, *MNRAS*, 474, 5372
- Erwin, P. 2019, *MNRAS*, 489, 3553
- Erwin, P. & Debattista, V. P. 2013, *MNRAS*, 431, 3060
- Erwin, P. & Sparke, L. S. 2003, *ApJS*, 146, 299
- Ferreira, L., Adams, N., Conselice, C. J., et al. 2022a, *ApJ*, 938, L2
- Ferreira, L., Conselice, C. J., Sazonova, E., et al. 2022b, *arXiv e-prints, arXiv:2210.01110*
- Finkelstein, S. L., Bagley, M. B., Haro, P. A., et al. 2022, *ApJ*, 940, L55
- Gadotti, D. A. 2009, *MNRAS*, 393, 1531
- Gadotti, D. A. 2011, *MNRAS*, 415, 3308
- Gadotti, D. A., Bittner, A., Falcón-Barroso, J., et al. 2020, *A&A*, 643, A14
- Gavazzi, G., Consolandi, G., Dotti, M., et al. 2015, *A&A*, 580, A116
- Guo, Y., Jogee, S., Finkelstein, S. L., et al. 2023, *ApJ*, 945, L10
- Herrera-Endoqui, M., Díaz-García, S., Laurikainen, E., & Salo, H. 2015, *A&A*, 582, A86
- Ho, L. C., Li, Z.-Y., Barth, A. J., Seigar, M. S., & Peng, C. Y. 2011, *ApJS*, 197, 21
- Jacobs, C., Glazebrook, K., Calabrò, A., et al. 2023, *ApJ*, 948, L13
- Jogee, S., Barazza, F. D., Rix, H.-W., et al. 2004, *ApJ*, 615, L105
- Jogee, S., Scoville, N., & Kenney, J. D. P. 2005, *ApJ*, 630, 837
- Kartaltepe, J. S., Rose, C., Vanderhoof, B. N., et al. 2023, *ApJ*, 946, L15
- Kim, T., Athanassoula, E., Sheth, K., et al. 2021, *ApJ*, 922, 196
- Knapen, J. H., Beckman, J. E., Heller, C. H., Shlosman, I., & de Jong, R. S. 1995, *ApJ*, 454, 623
- Kormendy, J. & Kennicutt, Robert C., J. 2004, *ARA&A*, 42, 603
- Kraljic, K., Bournaud, F., & Martig, M. 2012, *ApJ*, 757, 60
- Laurikainen, E., Salo, H., & Buta, R. 2005, *MNRAS*, 362, 1319
- Le Conte, Z. A., Gadotti, D. A., Ferreira, L., et al. 2024, *MNRAS*, 530, 1984
- Lee, Y. H., Ann, H. B., & Park, M.-G. 2019, *ApJ*, 872, 97
- Marinova, I. & Jogee, S. 2007, *ApJ*, 659, 1176
- Martinez-Valpuesta, I., Shlosman, I., & Heller, C. 2006, *ApJ*, 637, 214
- Masters, K. L., Nichol, R. C., Haynes, M. P., et al. 2012, *MNRAS*, 424, 2180
- Melvin, T., Masters, K., Lintott, C., et al. 2014, *MNRAS*, 438, 2882
- Menéndez-Delmestre, K., Sheth, K., Schinnerer, E., Jarrett, T. H., & Scoville, N. Z. 2007, *ApJ*, 657, 790
- Mortlock, A., Conselice, C. J., Hartley, W. G., et al. 2013, *MNRAS*, 433, 1185
- Moustakas, J., Lang, D., Schlegel, D. J., et al. 2021, in *American Astronomical Society Meeting Abstracts*, Vol. 53, American Astronomical Society Meeting Abstracts, 527.04
- Nair, P. B. & Abraham, R. G. 2010, *ApJS*, 186, 427
- Nelson, E. J., Suess, K. A., Bezanson, R., et al. 2022, *arXiv e-prints, arXiv:2208.01630*
- Oh, S., Oh, K., & Yi, S. K. 2012, *ApJS*, 198, 4
- Ohta, K., Hamabe, M., & Wakamatsu, K.-I. 1990, *ApJ*, 357, 71
- Pérez, I., Aguerri, J. A. L., & Méndez-Abreu, J. 2012, *A&A*, 540, A103
- Perrin, M. D., Sivaramakrishnan, A., Lajoie, C.-P., et al. 2014, in *Society of Photo-Optical Instrumentation Engineers (SPIE) Conference Series*, Vol. 9143, *Space Telescopes and Instrumentation 2014: Optical, Infrared, and Millimeter Wave*, ed. J. Oschmann, Jacobus M., M. Clampin, G. G. Fazio, & H. A. MacEwen, 91433X
- Postman, M., Franx, M., Cross, N. J. G., et al. 2005, *ApJ*, 623, 721
- Robertson, B. E., Tacchella, S., Johnson, B. D., et al. 2023, *ApJ*, 942, L42
- Rosas-Guevara, Y., Bonoli, S., Dotti, M., et al. 2022, *MNRAS*, 512, 5339
- Salo, H., Laurikainen, E., Laine, J., et al. 2015, *ApJS*, 219, 4
- Scoville, N., Aussel, H., Brusa, M., et al. 2007, *ApJS*, 172, 1
- Sheth, K., Elmegreen, D. M., Elmegreen, B. G., et al. 2008, *ApJ*, 675, 1141
- Sheth, K., Regan, M., Hinz, J. L., et al. 2010, *PASP*, 122, 1397
- Sheth, K., Regan, M. W., Scoville, N. Z., & Strubbe, L. E. 2003, *ApJ*, 592, L13
- Sobral, D., Smail, I., Best, P. N., et al. 2013, *MNRAS*, 428, 1128
- Stefanon, M., Yan, H., Mobasher, B., et al. 2017, *ApJS*, 229, 32
- Stone, C. J., Arora, N., Courteau, S., & Cuillandre, J.-C. 2021, *MNRAS*, 508, 1870
- van den Bergh, S., Abraham, R. G., Ellis, R. S., et al. 1996, *AJ*, 112, 359
- van der Wel, A., Franx, M., van Dokkum, P. G., et al. 2014, *ApJ*, 788, 28
- Wang, J., Athanassoula, E., Yu, S.-Y., et al. 2020, *ApJ*, 893, 19
- Wang, J., Kauffmann, G., Overzier, R., et al. 2012, *MNRAS*, 423, 3486
- Willett, K. W., Lintott, C. J., Bamford, S. P., et al. 2013, *MNRAS*, 435, 2835
- Xu, D. & Yu, S.-Y. 2024, *A&A*, 682, L17
- Yu, S.-Y., Cheng, C., Pan, Y., Sun, F., & Li, Y. A. 2023, *A&A*, 676, A74
- Yu, S.-Y. & Ho, L. C. 2020, *ApJ*, 900, 150
- Yu, S.-Y., Kalinova, V., Colombo, D., et al. 2022a, *A&A*, 666, A175
- Yu, S.-Y., Xu, D., Ho, L. C., Wang, J., & Kao, W.-B. 2022b, *A&A*, 661, A98
- Zhao, D., Du, M., Ho, L. C., Debattista, V. P., & Shi, J. 2020, *ApJ*, 904, 170